

INFRARED SPECTROSCOPY OF FAINT $15 \mu\text{m}$ SOURCES IN THE HUBBLE DEEP FIELD SOUTH: FIRST HINTS AT THE PROPERTIES OF THE SOURCES OF THE IR BACKGROUND

★ ★★

A. Franceschini¹, S. Berta¹, D. Rigopoulou², H. Aussel^{3,4}, C.J. Cesarsky⁵, D. Elbaz⁶, R. Genzel², E. Moy², S. Oliver⁷, M. Rowan-Robinson⁸, P.P. Van der Werf⁹

¹ Dipartimento di Astronomia, Vicolo Osservatorio 5, I-35122 Padova, Italy, E-mail: franceschini@pd.astro.it

² Max Planck Institute fuer Extraterrestrische Physik, Garching bei Muenchen, Germany

³ Osservatorio Astronomico di Padova, Italy

⁴ Institute for Astronomy, 2680 Woodlawn Drive, Honolulu, Hawaii 96822, USA

⁵ European Southern Observatory, Karl-Schwarzschild-str. 2, 85740 Garching, Germany

⁶ Centre d'Etudes de Saclay, Service d'Astrophysique, Orme des Merisiers, 91191 Gif-sur-Yvette, France

⁷ Astronomy Center, CPES, University of Sussex, Falmer, Brighton BN1 9QJ, UK

⁸ ICSTM, Astrophysics Group, Blackett Laboratory, Prince Consort Rd., London, SW2 1BZ, U.K.

⁹ Leiden Observatory, P.O. Box 9513, 2300 RA, Leiden, The Netherlands.

Received July 15, 2002/ Accepted

Abstract. We present a spectroscopic analysis of a sample of 21 galaxies with $z = 0.2\text{--}1.5$ drawn from a 25 square arcmin ultra-deep ISOCAM survey at $\lambda_{eff} = 15 \mu\text{m}$ centered in the WFPC-2 Hubble Deep Field South. Near-infrared spectra are reported for 18 ISO sources, carried out with ISAAC on the VLT, aimed at detecting the redshifted $H_\alpha + [\text{NII}]$. Additional optical data come from the ESO VLT/FORS2 and NTT/EMMI, primarily targeting $[\text{OII}]$, $[\text{OIII}]$ and H_β for further physical insight. Although not numerous in terms of areal density in the sky, this population of very luminous IR sources has been recently found to be responsible for a substantial fraction of the extragalactic background light energy density. H_α line emission is detected in virtually all the observed objects down to a flux limit of $7 \times 10^{-17} \text{ erg cm}^{-2} \text{ s}^{-1}$ (corresponding to $L_{H_\alpha} > 10^{41} \text{ erg s}^{-1}$ at $z = 0.6$ for $H_0 = 65$, $\Omega_\Lambda = 0.7$ and $\Omega_m = 0.3$). Our analysis (including emission line, morphology, and SED properties) shows clear evidence for AGN activity in only two of these sources: one type-I (with broadened H_α at $z=1.57$) and one type-II quasars (with inverted $[\text{NII}]/H_\alpha$ ratio at $z=1.39$), while we suspect the presence of an AGN in two further sources (an Ultra-Luminous IR Galaxy, ULIRG, at $z=1.27$ and a luminous galaxy at $z=0.69$). The H_α luminosities indicate star formation rates (SFR) in the remaining sources between 0.5 and 20 M_\odot/yr , assuming a Salpeter IMF between 0.1 and 100 M_\odot and without extinction corrections. We find good correlations between the mid-IR, the radio and H_α luminosities, confirming the mid-IR light as a good tracer of star formation (while the SFR based on H_α flux show some large scatter and offset, which are still to be understood). We have estimated the baryonic masses in stars with a newly-developed tool fitting the overall optical-IR continuum, and found that the host galaxies of ISO sources are massive members of groups with typically high rates of SF ($SFR \sim 10$ to 300 M_\odot/yr). We have finally compared this ongoing SF activity with the already formed stellar masses to estimate the timescales t_{SF} for the stellar build-up, which turn-out to be widely spread in these objects between 0.1 Gyrs to more than 10 Gyr. The faint ISOCAM galaxies appear to form a composite population, including moderately active but very massive spiral-like galaxies, and very luminous ongoing starbursts, in a continuous sequence. From the observed t_{SF} and assuming typical starburst timescales, we infer that, with few exceptions, only a fraction of the galactic stars can be formed in any single starburst event, while several of such episodes during a protracted SF history are required for the whole galactic build-up.

Key words. galaxies: interactions – starburst – Hubble Deep Field HDF – SED – spectroscopy.

1. INTRODUCTION

New populations of faint high-redshift sources have been recently discovered by deep mid- and far-IR surveys with the Infrared Space Observatory (e.g. Genzel & Cesarsky 2000, Aussel et al. 1999, Altieri et al. 1999, Elbaz et al. 1999, Rowan-Robinson et al. 1997) and by large millimetric telescopes at longer wavelengths (e.g. Smail et al. 1997, Hughes et al. 1998).

These sources display various distinct features compared with other optically selected galaxy populations. They are very luminous on average ($L_{bol} \geq 10^{11} L_{\odot}$, Elbaz et al. 2002), with the bulk of their emission coming out in the far-IR, in a similar way as the IRAS-selected galaxies include the most luminous systems in the local universe. On the contrary, their areal density (a few sources/square arcmin at the faintest limits detectable by ISO) is much lower than found for faint blue galaxies in the optical (e.g. Ellis 1997).

Another remarkable property of the faint IR-selected sources is to display extremely high rates of evolution with redshift, exceeding those measured for galaxies at other wavelengths and comparable or larger than the evolution rates observed for quasars (Hughes et al. 1998, Barger et al. 1998, Elbaz et al. 1999, 2002, Blain et al. 1999, Franceschini et al. 2001). This fast evolution of the IR sources implies that dust-obscuration, if moderately important in local galaxies where less than 50% on average of the optical-UV emission is absorbed, has strongly affected instead the past active phases of galaxy evolution.

Franceschini et al. (2001) and Elbaz et al. (2002) have matched the statistical and IR-spectral properties of the faint ISO sources detected at $\lambda_{eff} = 15 \mu\text{m}$ with the spectral intensity of the recently discovered Cosmic IR Background (CIRB, see Hauser et al. 1998, Puget et al. 1996). The CIRB appears to contain a large fraction (up to $\sim 70\%$, though this number is made uncertain by the optical-UV background intensity) of the total extragalactic background energy density from radio to X-rays, Cosmic Microwave Background excluded. These analyses have found that, due to their high luminosities and moderate redshifts ($z \simeq 0.5$ to 1.3), the faint $15 \mu\text{m}$ sources include the main contributors to the CIRB. This is a robust conclusion, based on the observed shape of the $15 \mu\text{m}$ counts, see Elbaz et al. 1999, and only assuming for these sources a typical IR galaxy SED. Then a large fraction of stars in present-day galaxies, or alternatively the bulk of degenerate baryons contained in nuclear supermassive BH's, have formed during IR-luminous dust-extinguished evolutionary phases.

The deep diffraction-limited observations at $15 \mu\text{m}$ with ISO provide quite an effective way of probing this

dust-obscured high-redshift activity. The numerous source samples detected in this way offer an important advantage over longer wavelength observations to allow easy optical identification, thanks to the relatively small error-box ($4.6''$ PSF, Okumura 1998) and the moderate redshifts and faintness of the optical counterparts.

We report here on optical and near-IR spectroscopic follow-up of a representative subset of the faint ISO population selected from a region centered in the HDF South. Apart from measuring the redshift, motivation for our observations was to clarify the nature of these objects: the main open issues were to assess the presence of energetically dominant AGNs as power sources, and to estimate the main physical parameters of the starburst and normal galaxy population, like the Star-Formation Rate (SFR), the extinction, and the stellar mass. Section 2 describes the IR-selected sample and the observations. Section 3 analyses the source properties based on the emission lines, while Section 4 those of the SEDs and continuum emission. Section 5 compares optical, near-IR, far-IR and radio indicators of SF and discusses the level of activity in the IR-selected galaxies. Section 6 summarizes our conclusions.

All quantities are computed assuming a universal geometry with $H_0 = 65 \text{ km s}^{-1} \text{ Mpc}^{-1}$, $\Omega_m = 0.3$, $\Omega_{\Lambda} = 0.7$. We indicate with the symbol S_{15} the flux density in Jy at $15 \mu\text{m}$ (and similarly for other wavelengths).

2. THE SAMPLE AND THE OBSERVATIONS

2.1. Sample selection

The Hubble Deep Field South was observed between October 17 and November 29, 1997, with the array camera ISOCAM onboard the Infrared Space Observatory, as part of the ELAIS collaboration (Oliver et al. 2000). The observations were carried out with two broad-band filters, LW2 (5-8.5 μm , $\lambda_{eff} = 6.75 \mu\text{m}$) and LW3 (12-18 μm , $\lambda_{eff} = 15 \mu\text{m}$). This followed a previous similar observing campaign on the HDF-North (Oliver et al. 1997), but adopted an improved observing strategy, particularly with LW2. The deep ISOCAM images with the two filters, obtained as repeated raster scans to improve the flat-field accuracy and time-redundancy, covered the same area centered on the HST WFPC-2 field. All details on the observations can be found in Oliver et al. (2002). We will consider in the following only the LW3 sample selected at $15 \mu\text{m}$ (for these sources we will also make use of $6.75 \mu\text{m}$ fluxes or upper limits from the LW2 observation).

Oliver et al. (2002) and Aussel et al. (2003) analyzed the ISOCAM data with two independent methods, accounting in detail for the time-varying signals under the effect of cosmic ray impacts. In particular, the method adopted by Aussel et al. makes use of a wavelet analysis of the combined spatial-temporal observable space (the PRETI method, see Stark et al. 1999, Aussel et al. 1999). The PRETI reduction has detected with LW3 63 sources brighter than $S_{15\mu\text{m}} = 90 \mu\text{Jy}$ (59 above $100 \mu\text{Jy}$) over an

* Based on observations with ISO, an ESA project with instruments funded by ESA member states (especially the PI countries: France, Germany, the Netherlands, and the United Kingdom) with the participation of ISAS and NASA.

** Based on observations collected at the European Southern Observatory, Chile, ESO No 63.O-0022, 65-000 67-000

Fig. 1. Image of the HDF–S region with indicated the LW3 15 μm sources (source labels refer to the catalogue by Aussel et al. 2003, see Tables 1 and following). Of the 86 objects indicated in this map, 63 belong to the complete sample with $S_{15} > 90\mu\text{Jy}$, while the other are fainter than this limit. The map is a collage by Hook (1999) including WFPC-2 F814 images in the Flanking Fields. The map scale is 4.7 arcminutes on a side. Contours represent the LW3 image depth, increasing towards the center.

area of 25 square arcminutes (for comparison, 24 of these sources appear in the shallower list by Oliver et al. within the inner 19.6 square arcmins). Detailed simulations have shown that above $S_{15\mu\text{m}} = 100 \mu\text{Jy}$ the PRETI sample is complete and free of spurious sources.

2.2. Source identification, target selection, photometric redshifts

We have compared the ISOCAM source lists with those from the Deep ESO Imaging Survey (EIS Deep), including optical imaging in UBVRi with ESO NTT/SUSI-2 down to limiting magnitudes of $U_{AB} \sim 27$, $B_{AB} \sim 26.5$,

$V_{AB} \sim 26$, $R_{AB} \sim 26$, $I_{AB} \sim 25$ and near-infrared JHK observations down to $J_{AB} \sim 25$, $H_{AB} \sim 24$, $K_{AB} \sim 24$ performed with NTT/SOFI (Da Costa et al. 1998). In addition we have used the optical catalogues in uBVRI by Teplitz et al. (1998), which has 5σ limiting magnitudes of $u \sim 24.5$, $B \sim 26.1$, $V \sim 25.5$, $R \sim 25.4$ and $I \sim 24$. Unfortunately, the EIS Deep images cover only a fraction ($\sim 70\%$) of the ISOCAM survey area.

<i>Obj.</i>	<i>R.A.</i>	<i>DEC.</i>	<i>U</i>	<i>B</i>	<i>V</i>	<i>R</i>	<i>I</i>	<i>J</i>	<i>H</i>	<i>K</i>	<i>LW2</i>	σ_{LW2}	<i>LW3</i>	σ_{LW3}
s14	22:32:41.52	-60:35:15.7	22.11	21.74	20.82	20.28	20.04	19.80	19.67	19.46	<0.143	0.143	0.239	0.044
s16	22:32:42.89	-60:32:10.9	22.57	22.38	22.00	21.35	21.07	20.81	20.73	20.42	<0.038	0.038	0.123	0.039
s19	22:32:43.51	-60:33:51.0	20.37	20.09	20.23	19.96	19.74	19.78	19.42	19.53	0.195	0.029	0.288	0.050
s20	22:32:44.11	-60:34:56.6	21.79	21.49	20.58	19.96	19.50	18.99	18.68	18.54	<0.053	0.053	0.164	0.041
s23	22:32:45.59	-60:34:18.4	24.90	24.11	22.17	21.42	20.78	19.84	19.26	18.94	0.118	0.023	0.749	0.097
s25	22:32:45.81	-60:32:25.7	24.14	23.43	22.73	21.88	21.37	20.27	19.80	19.58	<0.023	0.023	0.473	0.071
s27	22:32:47.70	-60:33:35.3	22.22	21.87	20.97	20.07	19.46	18.86	18.39	18.17	0.059	0.021	0.387	0.061
s28	22:32:47.61	-60:34:08.0	23.10	22.83	22.26	21.64	21.18	20.80	20.36	20.24	0.046	0.021	0.172	0.042
s38	22:32:53.13	-60:35:38.8	27.42	25.88	25.46	24.86	23.72	22.25	21.67	21.53	0.123	0.023	0.518	0.075
s39	22:32:53.06	-60:33:28.0	25.03	24.63	24.28	23.74	23.09	21.49	20.95	20.82	<0.015	0.015	0.226	0.043
s40	22:32:52.91	-60:33:16.6	25.98	25.20	24.78	24.15	23.49	21.99	21.34	21.09	<0.006	0.006	0.119	0.038
s43	22:32:53.75	-60:32:05.6	26.02	25.92	25.21	24.63	23.61	22.48	21.92	21.62	<0.015	0.015	0.095	0.035
s53	22:32:57.54	-60:33:05.5	22.03	21.84	21.32	20.66	20.27	19.87	19.47	19.29	0.038	0.021	0.338	0.056
s54	22:32:58.03	-60:32:04.2	24.89 [◊]	23.82 [◊]	22.54 [◊]	21.39 [◊]	20.18 [◊]	–	–	–	<0.046	0.046	0.129	0.039
s55	22:32:58.01	-60:32:33.8	23.76	23.47	22.71	21.99	21.33	20.61	20.05	19.88	<0.004	0.004	0.203	0.043
s60	22:33:01.79	-60:34:12.9	24.04	24.07	23.60	23.10	22.36	21.07	20.63	20.14	<0.025	0.025	0.097	0.036
s62	22:33:02.35	-60:35:25.3	23.61	23.36	22.97	22.33	21.81	20.94	20.67	20.60	<0.080	0.080	0.186	0.042
s72	22:33:05.91	-60:34:36.3	24.81 [◊]	23.70 [◊]	22.49 [◊]	21.34 [◊]	20.61 [◊]	19.89	19.27	18.94	0.079	0.021	0.370	0.059
s73	22:33:06.17	-60:33:50.3	19.33 [◊]	18.57 [◊]	17.73 [◊]	17.29 [◊]	16.86 [◊]	16.68	16.45	16.36	0.994	0.120	2.300	0.173
s79	22:33:08.89	-60:34:34.3	24.48 [◊]	24.38 [◊]	23.60 [◊]	22.99 [◊]	22.21 [◊]	21.63	21.11	20.78	<0.049	0.049	0.186	0.042
s82	22:33:12.42	-60:33:50.3	23.04 [◊]	22.80 [◊]	22.02 [◊]	21.17 [◊]	20.36 [◊]	20.11	19.98	20.01	0.179	0.027	0.475	0.071

[◊]: data from Teplitz et al. (1998)

Table 1. Available photometric data for the 15 μm sources in the HDF-S observed spectroscopically in the optical and near-infrared. Data are from the EIS Deep survey, but in highlighted cases for which the Teplitz et al. (1998) photometry is used. All magnitudes are in the AB system; ISOCAM LW2 and LW3 fluxes and uncertainties are reported in the last four columns. In the case only an upper limit is available, it is specified.

The spatial resolution of the ISOCAM images corresponds to a PSF of $4.6''$ (Okumura 1998). Within the ISOCAM errorbox, it turns out that there is almost invariably a galaxy relatively bright in the red wavebands (I,J,H,K). The procedures for optical identification are detailed in Mann et al. (2002) (see also Aussel et al. 1999).

Of the 63 sources in the PRETI LW3 sample, 24 are outside the JHK EIS coverage (10 of these are also outside the EIS optical imaging).

Of the other 39 sources, four are galactic stars, while for the remaining 35 objects the optical/near-IR coverage of the galaxy SED is detailed enough to allow a precise estimate of the redshift through fits with spectrophotometric models.

We selected the targets for the VLT/ISAAC spectroscopic follow-up from the HDF South LW3 source list based on the following criteria: a) H_α should be in the wavelength range covered by the ISAAC gratings, b) a secure counterpart should exist in the I or the K band images.

We did not apply any selection based on redshifts or colours, except to ensure that H_α was within the ISAAC spectral range. With these constraints, our reference sample reduces to 25 galaxies with $15 \mu\text{m}$ flux densities ranging between 95 and $800 \mu\text{Jy}$. It is thus a representative sample of the strongly evolving ISOCAM population near the peak of the differential source counts (Elbaz et al. 1999).

From these 25 sources we randomly selected 18 for the ISAAC follow up. For part of these and for 3 additional objects we have optical spectroscopic data.

The source list, coordinates, and the available optical, near-IR and mid-IR photometric data are reported in Table 1. Stamp images from the F814 WFPC-2 maps for each sources are reported in Appendix A, together with plots of the optical-IR SEDs and notes on the individual sources.

To set the ISAAC grating (Z, SZ, J, H) for H_α detections in our target sources, we used redshifts from optical spectra available for some of the objects at $z < 0.7$ (Dennefeld, private communication, see also Rigopoulou et al. 2000).

For all other sources we used photometric redshift estimates based on fits of the observed SEDs with synthetic galaxy spectra. In particular, we have used PEGASE (Fioc and Rocca-Volmerange 1997) and GRASIL (Silva et al. 1998) to construct grids of spectra as a function of galactic age, considering two evolutionary sequences: one describing a spiral-like evolutionary model with exponentially decreasing star-formation and long (5 Gyr) timescale, the other reproducing a more typical evolution for ellipticals with short (1 Gyr) exponential timescale and star-formation truncated by a galactic wind.

Since the main spectral feature of the SED suited for the redshift estimates is the Balmer 4000 \AA discontinuity, the effect of dust extinction on the redshift estimate is modest. The fit is automatically found from χ^2 interpolation on a 2D grid of redshift versus galactic age.

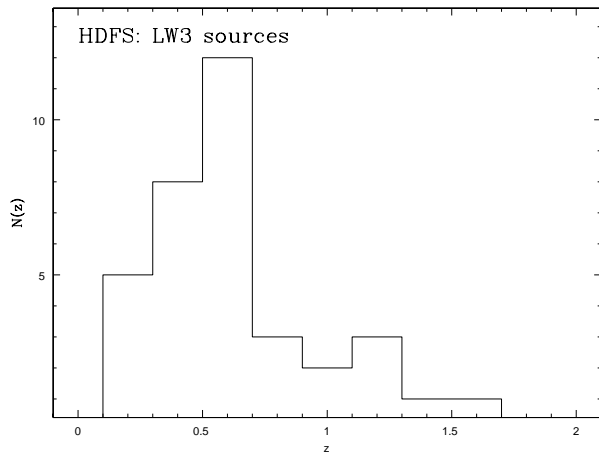


Fig. 2. The redshift distribution of faint ISOCAM LW3 sources in HDF South with optical identifications. The objects range between $z=0.2$ and 1.6 , mostly due to K-correction effects. Redshifts are spectroscopic when available, otherwise photometric.

Source	Run	PA	Grating
s16	1999	-49.99	SZ
s19	2000	75.42	H
s23	1999	63.45	Z
s25*	1999,2000	65.45	SZ
s27*	1999,2000	-43.85	SZ
s28	1999	-31.11	SZ
s38	1999	-77.41	H
s39	1999	29.45	H
s40	2000	-5.55	H
s43	2000	-56.05	J
s53	1999	67.22	SZ
s54	2000	10.25	J
s55*	1999,2001	-56.05	J
s60	1999,2000	-77.41	H
s62	2000	64.15	J
s72	2001	-67.35	SZ
s79	2000	11.57	J
s82	2000	110.30	J

*: high-res data ($R_s \sim 5000$) also exist.

Table 2. Summary of ISAAC/VLT observations. Slits have been rotated (anti-clockwise with respect to the North direction by the angle in column PA) in order to include the most interesting features of the sources.

After spectroscopic confirmation, our photometric redshift determinations turned out to be accurate to $\Delta z \approx \pm 0.1$. The fits based on the GRASIL and PEGASE codes provided essentially the same results in terms of redshifts. The distribution of redshifts for the ISOCAM LW3 sample in the HDF South is shown in Fig. 2. The objects range between $z=0.2$ and 1.6 , an interval mostly imposed by K-correction effects (e.g. Franceschini et al. 2001): at $z \sim 0.6 - 0.8$ the $7.7 \mu\text{m}$ PAH emission feature usually very intense in starburst galaxies falls within the LW3 fil-

ter. The z distribution shows a strong peak at $z \simeq 0.6$ probably due to a cluster or a large galaxy concentration in the HDF South. This overdensity is also apparent in the analysis of photometric redshifts by Rudnick et al. (2001). This z distribution is remarkably different from that of ISOCAM sources at similar depths in the HDF North (Aussel et al. 1999), particularly in lacking the peak at $z \sim 0.8 - 1$. The effect of cosmic variance is very prominent between the two fields.

2.3. IR spectroscopic observations and data reduction

We collected the IR spectra during three runs (September 1999, August 2000 and 2001) using the infrared spectrograph ISAAC (Moorwood et al. 1998) on the ESO ANTU telescope (formerly UT1), on Paranal, Chile. The observing logs are summarized in Table 2.

Observations have been performed with the Low Resolution grating, providing a spectral resolution $R_s \sim 600$ for a slit width of $1''$ (the length is fixed to $2'$). Four of our sample objects (S55, S27, and an interacting pair associated with source S25) were also observed during the 2000 and 2001 runs with the Medium-Resolution gratings ($R_s \sim 5000$) (Rigopoulou et al. 2002).

To maximize the observing efficiency, whenever possible the slit position included two target galaxies at any given orientation. Most of the targets were first acquired directly from a 1–2 min exposure in the H-band. In the case of the very faint objects ($H > 20.0$ mag), we blind-offset from a brighter star in the HDF-S field. Observations were made by nodding the telescope $\pm 20''$ along the slit to facilitate sky subtraction (always avoiding overlap of the two objects in the slit). Individual exposures range from 120 (in H and J bands) to 300 (SZ band) seconds. During the 1999 and 2000 runs, sky conditions were excellent throughout the acquisition of the spectra, with seeing values typically in the range $0.4''-0.8''$ and dipping down to $0.25''$. For each filter, observations of spectroscopic standard stars were made in order to flux calibrate the galaxy spectra.

The data were reduced using applications in the ECLIPSE (Devillard 1998) and IRAF¹ packages. Accurate sky subtraction is critical to the detection of faint lines. Sky was removed by subtracting the pairs of offset frames. In some cases this left a residual signal (due to temporal sky changes) which was then removed by performing a polynomial interpolation along the slit. OH sky emission lines were also carefully removed from the spectra. Spectrum extraction for each galaxy was performed using the APEXTRACT package. Standard wavelength calibration was applied.

The ISAAC spectra have been flux-calibrated using standard infrared stars from Pickles (1998) and

¹ The package IRAF is distributed by the National Optical Astronomy Observatory which is operated by the Association of Universities for Research in Astronomy, Inc., under cooperative agreement with the National Science Foundation.

van der Blik et al. (1996). The near-infrared spectra from the 1999 run have appeared in Rigopoulou et al. (2000). Here we present in Figure 3 the ISAAC spectra from the 2000 and 2001 runs, while the measured fluxes are summarized in Table 3.

2.4. Complementary optical spectroscopy

To add further constraints on the nature of the 15 μm source population, particularly to estimate dust-extinction from Balmer line ratios, two different sets of ground-based optical spectroscopic observations have been analyzed.

Tresse et al. (1999) observed the region around QSO J2233–606, which is in the STIS HDF–South, with the ESO Multi Mode Instrument (EMMI, D’Odorico 1990) at NTT, during the nights between September 23th and 25th and October 17th to 19th 1998. The data were obtained in Multi Object Spectroscopy (MOS) mode, with different pointings and masks, for a total of 6 sets and roughly 200 slit positions. Tresse et al. (1999) chose slits with $1.02''$ or $1.34''$ width and spectral resolutions of 10.6 and 13.9 \AA in the I band (centered at 7985 \AA).

We also obtained observations with FORS2 (Appenzeller et al. 2000) at VLT/UT2 in MOS configuration, during the FORS2 commissioning phase, between December 22, 1999, and January 5, 2000. The 300I grism with a dispersion of $2.5\text{\AA}/\text{pixel}$ between 6000 and 11000 \AA and a $1''$ -wide slit were used. A few of the ISOCAM targets in our list have been included by chance in this spectroscopic survey.

Both EMMI and FORS2 data were reduced with the standard IRAF’s tasks. Pre-reduction (bias subtraction and flat-fielding), extraction and wavelength calibration were performed with the usual procedure. EMMI data were flux-calibrated using stars from Stone & Baldwin (1983) and Baldwin & Stone (1984), observed within each mask. Unfortunately, for FORS2 observations no data on standard stars were available. However, two stars have been included in the MOS HDF–South frames: after identification in the EIS catalogue, the spectral data were calibrated by imposing to the observed stellar spectra to reproduce the I-band fluxes, after convolution with the instrument response function reported in the ESO exposure–time calculator.

Optical spectra with EMMI are reported in Figure 4.

3. SOURCE PROPERTIES BASED ON THE EMISSION LINES

The ISAAC near-IR spectroscopy has been targeted to detect the redshifted H_α line, while optical observations with EMMI and FORS2 have allowed the study of the rest-frame emission lines up to $\sim 5000\text{\AA}$.

Table 3 summarizes the properties of reliable line detections with the three instruments. The columns report, in the order, the source identification, the instrument, integration times, the measured fluxes of $[\text{OII}]\lambda 3727$, H_β ,

#	Object			[OII]		H β		[OIII]		H α (+[NII])	
	Instr.	t_{exp}	z	S	EW	S	EW	S	EW	S	EW
s14	EMMI	5400s	0.41	19.4	26	9.55	10	6.64	7		
s16 [†]	ISAAC	3720s	0.62							11.7	45
s19	ISAAC	5760s	1.57							157	816
s20	EMMI	5400s	0.39	17.2	37	7.30	7				
s23	EMMI	8100s	0.46	13.7	28	3.23	9	6.04	16		
s23 [†]	ISAAC	3720s	0.46							18.6	50
s25	EMMI	5400s	0.58			4.90	18				
s25	FORS2	17380s	0.58			5.64	28				
s25 [†]	ISAAC	3720s	0.58							31.2	110
s27	FORS2	15340s	0.58			6.03	4				
s27	FORS2	18000s	0.58			7.39	6				
s27 [†]	ISAAC	3720s	0.58							32.82	47
s28 [†]	ISAAC	3720s	0.58							7.8	47
s38 [†]	ISAAC	7400s	1.39							19.5	35
s39 [†]	ISAAC	7400s	1.27							71.3	67
s40	ISAAC	3860s	1.27							13.1	67
s40	ISAAC	5760s	1.27							13.6	95
s43	ISAAC	4320s	0.95							38.6	13
s53(I)	EMMI	7200s	0.58	11.6	39	12.0	30				
s53(I)	FORS2	18000s	0.58			16.7	33				
s53 [†]	ISAAC	3720s	0.58							60.8	70
s55	FORS2	18000s	0.76			3.94	28				
s55	ISAAC	3840s	0.76							30.7	67
s55 [†]	ISAAC	3720s	0.76							24.1	40
s60 [†]	ISAAC	7400s	1.23							27.3	44
s62 [†]	ISAAC	3720s	0.73							25.4	62
s72	ISAAC	1800s	0.55							53.5	111
s73	FORS2	18000s	0.17							224	32
s79	ISAAC	3840s	0.74							13.2	65
s82	ISAAC	3840s	0.69							33.2	26

[†]: data from Rigopoulou et al. (2000)

Table 3. Summary of results of spectroscopic observations. We report the source name, the instrument, the exposure time, spectroscopic redshift, the measured fluxes (in units of 10^{-17} erg cm $^{-2}$ s $^{-1}$) and equivalent widths (EW, in Å) of [OII] λ 3727, H β (λ 4861), [OIII] λ λ 4959, 5007, and H α (λ 6563). H α fluxes and EW of H α + [NII] are from Rigopoulou et al. (2000). These measured line fluxes are not corrected for aperture.

[OIII] λ λ 4949, 5007, H α + [NII]. The Table includes revised fluxes from the Rigopoulou et al. (2000) observations. However, only the extremely good seeing conditions of the 1999 observing run have allowed the separation of the [NII] from H α for some of the sources. The corresponding separate fluxes for the resolved lines are reported in Rigopoulou et al. (2000). If an object was detected in different runs, both results are shown. Uncertainties on the measured fluxes are of the order of 10%.

3.1. Aperture corrections

We have applied aperture correction factors to account for the light missed due to our finite 1'' size slit. We have calculated different correction factors for unresolved (source sizes $\leq 1''$) and resolved sources (size $\geq 1''$).

For the unresolved sources we applied an average correction factor of 1.15 which was calculated as follows. We have smoothed the WFPC2 F814 image of the galaxies

to a resolution of 0.6'' (to simulate the seeing during the observations) and measured the ratio between the total source counts and the counts through an artificial 1'' slit.

For the resolved sources (S27, S28, S53 and S55) aperture corrections have been calculated with two different methods.

(1) We used the WFPC2 F814 image (smoothed as before to a resolution of 0.6'' to account for the seeing) and carried out aperture photometry for various aperture sizes (which allowed us to probe the distribution of the flux and the source size in the sky). We then calculated the flux through an artificial 1'' slit oriented along the same PA as for the observation. The average ratio between the total flux and that within the 1'' slit gave us an average correction factor of ~ 1.7 .

(2) As a check, we have compared the broad band magnitudes in the z and J bands (corresponding to the H α rest-wavelength for $z \sim 0.8$ and $z \sim 0.6$, respectively) with the total observed H α line flux emitted by the sources.

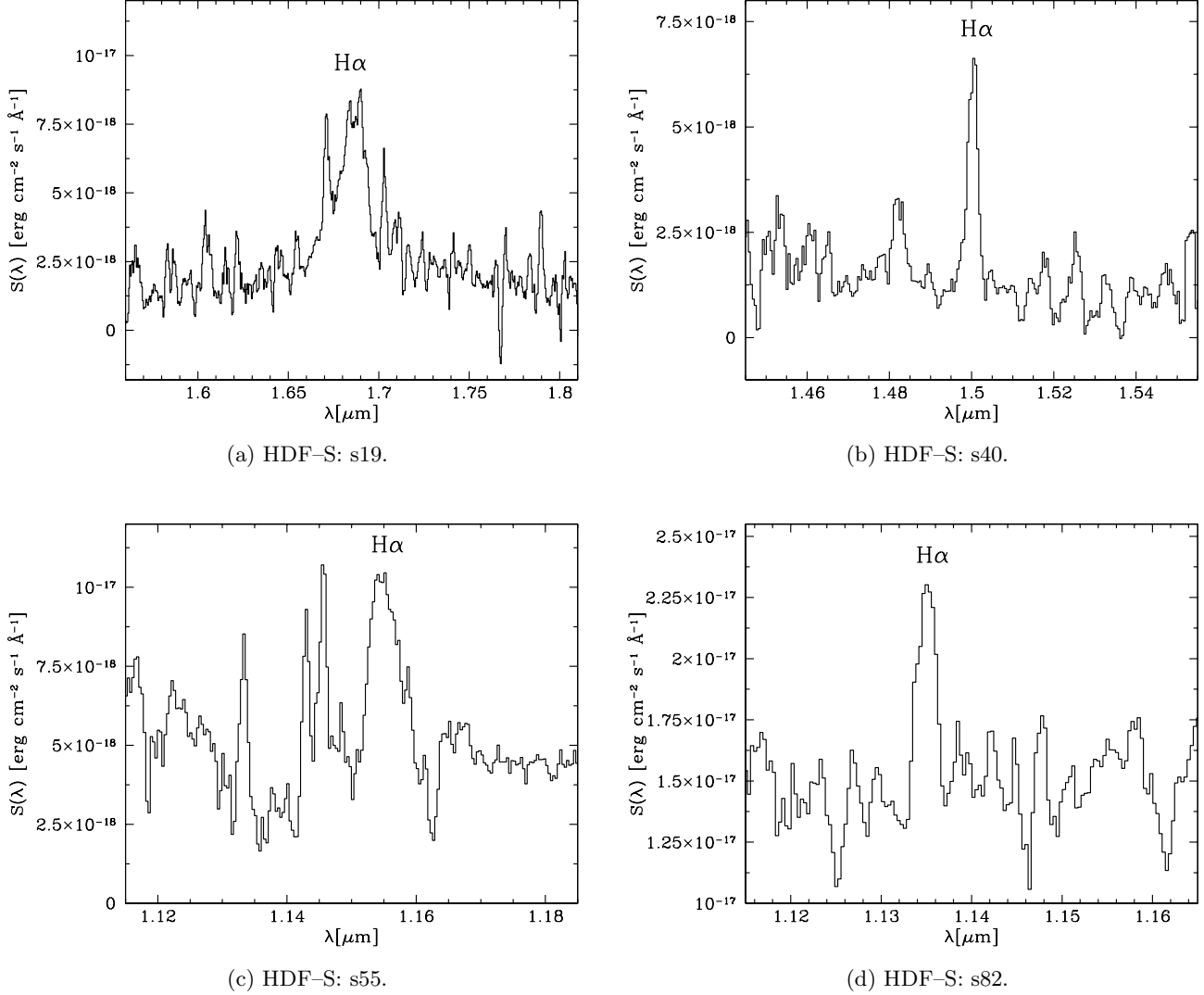


Fig. 3. Spectra of the 15 μm sources in the HDF-S observed with ISAAC at the VLT.

Since we cannot estimate the line-to-continuum ratio from our spectra due to the low continuum signal, the ratio of the broad-band flux to the $\text{H}\alpha$ flux provides a conservative upper limit to the aperture correction.

The correction factors that we obtained in this way are ~ 2 on average for the four sources, consistent with the previously estimated average value. In what follows we used correction factors of 1.15 for the unresolved and 1.7 for the resolved sources.

3.2. Evidence for AGN contributions to the line emission

A primary motivation for our spectroscopic follow up of the faint ISO sources was to determine to what extent the luminous IR emissions are contributed by AGNs, and how much by young stars. To this end, the observed optical and IR spectra have been used to identify broad lines components and anomalous line flux ratios.

Our search for broad permitted lines was limited by the low spectral resolution of the ISAAC spectra, and even more by the low signal-to-noise ratio preventing reliable setting of the underlying continuum. The spectral resolving power of $R_s \simeq 600$ corresponds to a rest-frame resolution of 12\AA at $z=0.6$ and a velocity threshold of ~ 250 km/s for the ISAAC Low-Resolution gratings. For the Medium-Resolution grating the resolving power corresponds to ~ 40 km/s. Consequently, for 16 out of 20 ISO sources in our sample observed at low-resolution, only broad-line components ($v > 1000$ km/s) can be resolved in principle. For S14, S20 and S23 we have good quality optical NTT/EMMI spectra with resolving power $R_s = 580$ (~ 500 km/s).

We report in Table 4 the half-power widths of the relevant permitted lines based on both IR and optical spectra. Only for one source (S19) these imply velocity fields significantly in excess of 1000 km/s (indicative of the presence of an AGN). For four more sources with $\text{H}\alpha + [\text{NII}]$ line

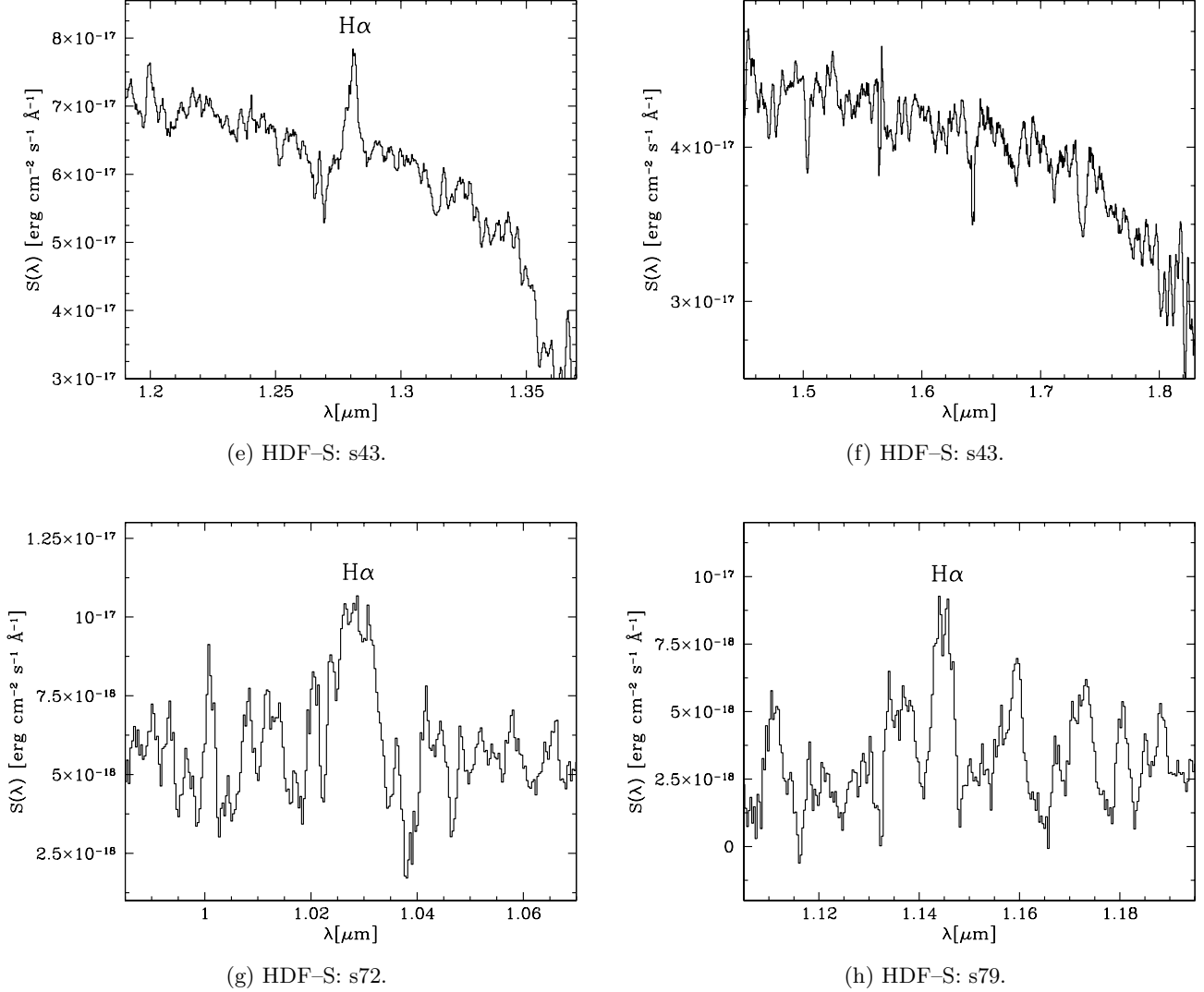


Fig. 3: continues.

widths also formally in excess of 1000 km/s, the poor S/N and the unresolved [NII] contribution prevent a reliable measure of the velocity field. In all other cases the line widths are consistent with those typical of massive starburst galaxies.

The $H\alpha$ to [NII] flux ratio may be used in principle as an indicator of the ionization field in the source. However, because of our limited resolving power, the line complex was resolved for only 3 sources of the 1999 run (Rigopoulou et al. 2000). Interestingly, one of these (S38 at $z=1.39$) reveals an inverted line ratio ($H\alpha/[NII]\simeq 0.8$), together with a moderately broadened $H\alpha$ (~ 600 km/s, see Table 4).

No evidence for broad components or peculiar $H\alpha/[NII]$ flux ratios was found in the optical counterparts to S25, S27 and S55 observed in the ISAAC Medium-Resolution mode, whose spectra are consistent with those of standard spiral and starburst galaxies with no AGN signatures (Rigopoulou et al. 2002).

Altogether, two out of 21 of the faint ISO sources in our spectroscopic survey reveal evidence for either type-I (source S19) or type-II (source S38) AGN activity. These indications from line measurements will be compared in Sect.4.2 with those coming from the study of the optical-IR-radio continuum SEDs.

3.3. Estimates of dust extinction from line ratios

Corrections of the $H\alpha$ flux for dust extinction are needed when using the line fluxes to estimate the rates of star formation. These are usually computed from the observed ratios of the Balmer lines compared with theoretical models of atomic transitions and nebular emission. Hummer & Storey (1987) report the ratios of emission lines based on Case B recombination theory for $T = 10000$:

$$\frac{I(H\alpha)}{I(H\beta)} = 2.85.$$

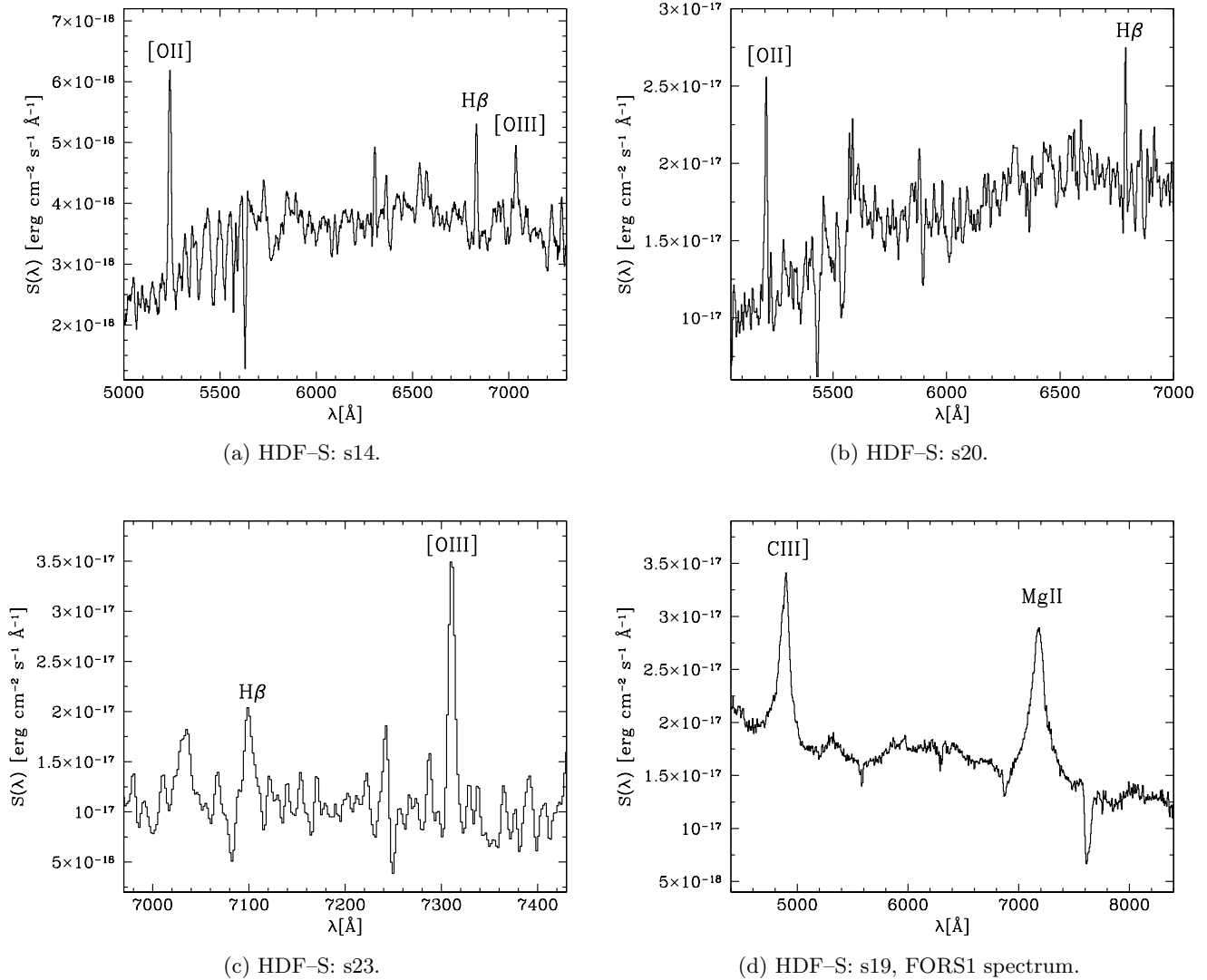


Fig. 4. Observed optical spectra: panels (a) to (c) show $15\ \mu\text{m}$ sources observed at NTT/EMMI. Panel (d) represents the QSO *s19* from FORS1/VLT: the two bright broad lines are $\text{MgII}\lambda 2798$ and $\text{CIII}\lambda 1908$, redshifted at $z \simeq 1.56$ (courtesy of Rigopoulou et al., 2002, in preparation).

By comparing this value with the observed line ratios and using a standard extinction law (Fitzpatrick, 1999), we obtain the A_V values reported in Table 5. The same Table also includes the extinction values based on fits of spectrophotometric models to the optical/near-IR SEDs, as explained in Sect. 4.1.

All A_V values turn out to be greater than 1.5 magnitudes, implying substantial amounts of dust extinction in these objects, which are not typical of normal quiescent spirals for which $A_V \simeq 0.3 - 0.5$. If anything, these estimates are likely to be lower limits, since this indicator based on Balmer line ratios quickly saturates in a mix of dust and radiative sources.

3.4. Estimates of the Star Formation Rate

Nebular emission lines, such as $\text{H}\alpha$, are generated in the interstellar medium, ionized by the ultraviolet continuum of the young stars recently formed in the starburst (those with ages $\leq 10^7$ yrs). These lines then provide a direct indication of the rate of the ongoing stellar formation.

The conversion factor between ionizing flux and SFR may be computed with an evolutionary synthesis model, assuming solar abundances, a Salpeter IMF ($0.1-100\ M_\odot$) and for continuous bursts with duration in the range between $\text{few} \times 10^7$ yrs to $\text{few} \times 10^8$ yrs. We adopt for this the Kennicutt (1998) relation:

$$\frac{\text{SFR}}{M_\odot \text{yr}^{-1}} = 7.9 \cdot 10^{-42} L_{\text{H}\alpha} (\text{erg s}^{-1}), \quad (1)$$

which we used to derive the values of ongoing SFR in the HDF-S objects with reliable $\text{H}\alpha$ detections. After conver-

Obj. id.	line meas.	FWHM [Å]	FWHM [km/s]	Threshold velocity
s14	H β	11	481	300
s19	H α	261	4642	400
s20	H β	10	443	300
s23	H β	14	591	400
s25	H β	10	390	200
s27	H α	8	231	300
s38	H α	32	612	250
s39	H α	70	1200	450
s40	H α + [NII]	25	503	350
s43	H α + [NII]	50	<1172	-
s55	H α + [NII]	50	<1299	-
s60	H α + [NII]	18	368	300
s62	H α + [NII]	19	502	500
s72	H α + [NII]	84	<2477	-
s79	H α + [NII]	27	709	500
s82	H α + [NII]	26	703	500

Table 4. Widths of relevant emission lines from ISAAC Low-Res and optical spectroscopy. The source name, reference line used for the measure, FWHM in Å, FWHM in km/s, and the threshold resolving power in km/s are reported.

Obj. #	L^* (H α)	SFR (H α)	A_V (col.)	A_V (spec.)	SFR (H α), corr
16 [†]	0.251	1.983	1.00	-	3.935
23 [†]	>0.194	>1.532	2.40	1.84	>5.405
25 [†]	0.569	4.495	-	2.10	18.964
27 [†]	0.867	6.856	1.98	1.69	21.874
28 [†]	0.191	1.504	1.20	-	3.423
38 [†]	3.060	24.185	2.60	-	143.865
39 [†]	8.930	70.541	2.45	-	378.465
40	1.678	14.479	-	-	-
43	2.358	18.630	2.36	-	93.955
53 [†]	1.622	12.819	1.42	2.05	52.443
55 [†]	1.234	9.751	1.83	2.63	59.125
60 [†]	3.158	24.944	2.25	-	116.725
62 [†]	0.812	6.414	1.40	-	16.756
72	0.858	6.782	-	-	-
73	0.207 [×]	1.635	-	-	-
79	0.436	3.449	-	-	-
82	0.984	7.773	-	-	-

[†]: H α fluxes from Rigopoulou et al. (2000)

*: H α luminosities in units of 10^{42} erg s $^{-1}$

×: S73, no aperture correction performed.

Table 5. Relevant spectroscopic data: aperture-corrected H α luminosities, rates of star formation based on H α , and extinction estimates from the Balmer decrement. In the fourth column we report extinction values based on photometric fits with spectral synthesis codes (see Sect. 4.1) and values of SFR corrected for slit-aperture and reddening (from Balmer lines when available). SFRs are in M_{\odot} yr $^{-1}$.

sion from fluxes to luminosities and after applying slit-aperture and extinction corrections, SFRs were calculated from eq. (1) and reported in Table 5.

Obj #	z	L_{IR} L_{\odot}	SFR $[M_{\odot} \text{ yr}^{-1}]$	M $[10^{11} M_{\odot}]$	M range $[10^{11} M_{\odot}]$
14	0.41	$5.8 \cdot 10^{10}$	10.0	0.32	0.20÷0.40
15	(0.55)	$1.8 \cdot 10^{11}$	30.6	3.10	2.30÷3.10
16	0.62	$8.7 \cdot 10^{10}$	14.9	0.29	0.21÷0.33
18	(0.55)	$1.4 \cdot 10^{11}$	23.4	5.20	5.00÷5.50
19	1.57	$1.4 \cdot 10^{12*}$	-	-	-
20	0.39	$3.5 \cdot 10^{10}$	6.0	0.80	0.55÷1.28
23	0.46	$2.9 \cdot 10^{11}$	50.2	0.97	0.42÷1.50
25	0.58	$3.3 \cdot 10^{11}$	56.0	0.80	0.50÷1.20
27	0.58	$2.6 \cdot 10^{11}$	44.8	4.70	3.90÷5.70
28	0.58	$9.6 \cdot 10^{10}$	16.5	0.40	0.25÷0.70
30	(0.40)	$2.7 \cdot 10^{10}$	4.6	0.01	0.005÷0.020
36	(0.65)	$2.7 \cdot 10^{11}$	46.3	0.40	0.20÷0.60
38	1.39	$1.3 \cdot 10^{12*}$	-	1.40	1.00÷3.00
39	1.27	$4.4 \cdot 10^{12}$	748.9	1.70	1.00÷3.20
40	1.27	$1.5 \cdot 10^{12}$	264.9	1.20	0.70÷3.00
41	(0.30)	$1.6 \cdot 10^{10}$	2.7	0.055	0.045÷0.069
43	0.95	$3.3 \cdot 10^{11}$	57.5	0.50	0.20÷1.00
45	(0.65)	$3.9 \cdot 10^{11}$	66.6	0.80	0.40÷1.60
48	(0.30)	$1.6 \cdot 10^{10}$	2.8	0.10	0.06÷0.20
52	(0.60)	$1.2 \cdot 10^{11}$	20.1	0.13	0.11÷0.16
53	0.58	$2.2 \cdot 10^{11}$	38.5	1.20	1.00÷1.50
55	0.76	$2.6 \cdot 10^{11}$	45.4	1.30	0.60÷1.60
60	1.23	$9.7 \cdot 10^{11}$	167.2	2.50	1.60÷4.00
62	0.73	$2.2 \cdot 10^{11}$	36.9	0.66	0.35÷0.90
67	(1.00)	$1.4 \cdot 10^{12}$	244.3	0.34	0.21÷0.60
71	(0.45)	$2.6 \cdot 10^{10}$	4.4	0.04	0.015÷0.060
72	0.55	$2.2 \cdot 10^{11}$	36.9	1.40	1.10÷1.80
73	0.17	$8.0 \cdot 10^{10}$	13.7	1.50	0.90÷1.90
75	(0.45)	$1.5 \cdot 10^{11}$	25.0	1.30	0.93÷1.60
77	(0.40)	$6.9 \cdot 10^{10}$	11.8	0.80	0.48÷1.15
79	0.74	$2.2 \cdot 10^{11}$	38.4	0.60	0.30÷1.20
82	0.69	$5.2 \cdot 10^{11}$	90.2	0.50	0.22÷1.10
85	(0.40)	$2.8 \cdot 10^{10}$	4.7	5.70	5.20÷6.00

* Based on the AGN model described in Appendix A.

Table 6. Values of the baryonic masses, SFRs and bolometric IR ($8 \div 1000 \mu\text{m}$) luminosities of the 15 μm sources in the HDF-S, as derived from the analysis of their spectral energy distributions (see Sects. 4.3 and 4.4).

4. SOURCE PROPERTIES BASED ON THE CONTINUUM EMISSION

The extensive spectral coverage of our source SEDs between the UV and the far-infrared (including the radio flux for a few) allows adding very significant constraints on the physical processes taking place inside them.

For typical IR galaxies the bulk of stellar formation happens inside dust-rich and optically thick molecular clouds, absorbing the UV-optical continuum emitted by luminous young stars and re-emitting it in the infrared. Given the large extinction values, the optical to near-IR continuum spectrum is moderately influenced by the starburst and includes important contributions by the less-extinguished older stellar populations (e.g. Poggianti, Bressan, Franceschini 2001). On the contrary, the mid- and far-IR spectrum is typically dominated by thermal emission by dust mostly illuminated by the young stars (the radio flux is also proportional to the number of recently born massive stars).

As a consequence, our capability to cover simultaneously the whole SEDs up to the far-IR provides a unique opportunity to sample all stellar generations and ages in these galaxies, and in particular to compare the mass fractions in old stars (the inactive, passively evolving compo-

ment) to those of newly formed stars (the "active" component), hence to evaluate the "activity" level in these galaxies.

SEDs and (when available) WFPC-2 images of our sample sources are reported in Figs. A.2 and A.3, together with spectral fits based on GRASIL, and with the SEDs of template galaxies used for comparison. The dot-dashed line in each panels, in particular, corresponds to the SED of M51, which we assumed to represent the prototype inactive spiral: the comparison of this template, scaled to fit the near-IR spectrum, with the ISO data at 6.7 and 15 μm shows that quite often the observed mid-IR fluxes are in excess by a substantial factor. Assuming that this excess IR emission is due to the starburst, this factor may be taken as a measure of the level of "activity" in the ISO galaxies.

Additional contributions to the source fluxes - further enhancing this "activity" level - may come from nuclear non-thermal emission of gravitational origin, an AGN component.

4.1. Estimates of dust extinction based on the continuum

The lack of information on the Balmer line ratios for several of our sample sources has forced us to look for alternative methods to estimate the dust extinction. A widely used one is to exploit colour indices. Using the codes of spectrophotometric synthesis GRASIL (Silva et al., 1998) and STARS (Sternberg 1998, Thornley et al. 2000) we have generated a grid of models for various star formation histories and bursts of different duration, and calculated the intrinsic (dust-free) V-K colours (typically varying in the range V-K = 1.1-1.5). We have then applied infrared and optical K-corrections from Poggianti (1997) and Coleman (1980), respectively. By comparing the observed and model predicted V-K colours, we obtained a median A_V of 1.8, assuming a screen model for the extinction. We stress that the extinction estimates based on the V-K colour represent a global (galaxy-wide) extinction which may not necessarily represent the extinction towards the deeply embedded young stars where most of the line emission originates. Note that, although somewhat more physically motivated, a model with homogeneous mix of dust and stars could not provide a fit to the optical spectrum: at increasing the intrinsic dust optical depth the extinction saturates to $A_V \simeq 0.7$ (e.g. Poggianti, Bressan, Franceschini 2001), a value not large enough to explain our typical source spectra.

Alternatively, we can estimate the extinction based on the rest-frame $L_{UV}(2800)$ continuum. Values of L_{UV} have been interpolated from B V I colours, using grids of synthetic models as described above, with constant star formation rate. The median $L_{UV}(2800)$ for the present ISOHDF-S sample is $1.47 \times 10^{40} \text{ erg s}^{-1} \text{ A}^{-1}$. For the same

IMF as assumed before, we find the following relation between the SFR and $L_{UV}(2800)$:

$$SFR(M_{\odot}/yr) = 1.88 \times 10^{-40} L_{UV}(2800)(\text{ergs}^{-1} \text{ A}^{-1}). \quad (2)$$

The ratio between the H_{α} and UV-based SFRs turns out to be $SFR(H_{\alpha})/SFR(2800) \sim 4.0$. For the corresponding extinction it follows that $A(H_{\alpha}) = 0.76 A_V$ and $A(UV) = 1.6 A_V$ (Pei 1992). We then deduce that, for a screen distribution, the extinction is $A_V \sim 1.6$. This extinction corresponds to a correction factor for the $SFR(H_{\alpha})$ of ~ 3 .

4.2. Disentangling AGN from starburst signatures in the UV-optical-IR-radio SEDs

The mid-IR spectra of galaxies are a complex mixture of various components. Typically the most important one is the emission by molecular complexes (probably Polycyclic Aromatic Hydrocarbons, PAH, see Puget & Leger 1989, but their nature is still uncertain) producing bands at 6.2, 7.7, 8.6 and 11.3 μm on top of a hot dust continuum. The PAH emission is particularly prominent in star-forming galaxies. Both the continuum intensity and the PAH's equivalent widths are sensitive to the presence of an AGN: while the AGN luminous point-like source enhances the hot-dust continuum emission, the PAH molecules tend to be destroyed by the intense radiative field and the corresponding emission bands become weaker (Lutz et al. 1998, Rigopoulou et al. 1999, Tran et al. 2001).

Therefore starburst-dominated and AGN-dominated galaxies tend to display different mid-IR spectra. The former show a bumpy spectrum with prominent emission features at $\lambda > 6 \mu\text{m}$ and a steeply decreasing flux shortwards of 6 μm , due to the moderate intensity of the radiative field and to the lack of very hot dust. A typical starburst spectrum is reported in Figs. A.2 and A.3 as the thick continuous line, corresponding to the SED of the galaxy M82.

On the contrary, AGN-dominated sources show rather flat mid-IR spectra, with almost absent PAH features and strong emission by very hot dust detectable down to few microns (a comparison of the spectrum of the Seyfert galaxy NGC 1068 with those of starbursts is reported in Aussel et al. 1999 and Elbaz et al. 2002).

The shape of the mid-IR spectrum can then in principle be used to disentangle between the two power mechanisms. In our case we can exploit the ratio of the LW3 to LW2 fluxes as a measure of how fast the rest-frame SED drops at $\lambda < 6 \mu\text{m}$ for sources at $z > 0.4$: while this flux ratio is expected to be ≥ 4 for starbursts as a consequence of the LW2 flux missing the redshifted PAH and dust emissions, the ratio becomes $\frac{S(LW3)}{S(LW2)} \leq 4$ in the case of an AGN-dominated source. Two such sources in Fig. A.2 are S19 and S38, having respectively $\frac{S(LW3)}{S(LW2)} \simeq 1.5$ and 2.3. For a third source, S82, the flux ratio is also low, $\frac{S(LW3)}{S(LW2)} \simeq 2.6$, and this could also be a type-II quasar. In

all other cases, either LW2 has no detection or the flux ratio falls in the starburst regime.

Note that this starburst/AGN discriminant would not work for sources at $z < 0.4$: an example is S73, showing a low $\frac{S(LW3)}{S(LW2)} \simeq 2$ value only because its low redshift ($z=0.17$) prevents the PAH bundle to be redshifted out of the LW2 band.

Radio data could in principle add valuable information to the SED analysis. On one side, given the tight radio/far-IR correlation for star-forming galaxies (Helou, Soifer and Rowan-Robinson 1985), the radio flux may provide an independent estimate of the bolometric luminosity and star formation rate. On the other side, a substantial excess of radio emission above the value pertaining to the radio/far-IR relation may be taken as evidence for emission by an AGN.

Unfortunately, for only a handful of the HDF South sources data at 1.4, 2.5, 4.9 and 8.6 GHz are reported by Mann et al. (2002) based on ATCA observations. Of the four radio-detected sources in our sample, S19 was already identified as a bona-fide type-I quasar, while S39 was suspected to include an AGN contribution based on the broadness of the H_α line and morphology (see the Appendix). For S39 the 1.4 GHz radio emission is however consistent with the radio/far-IR relation for starbursts (see Fig. 9 below).

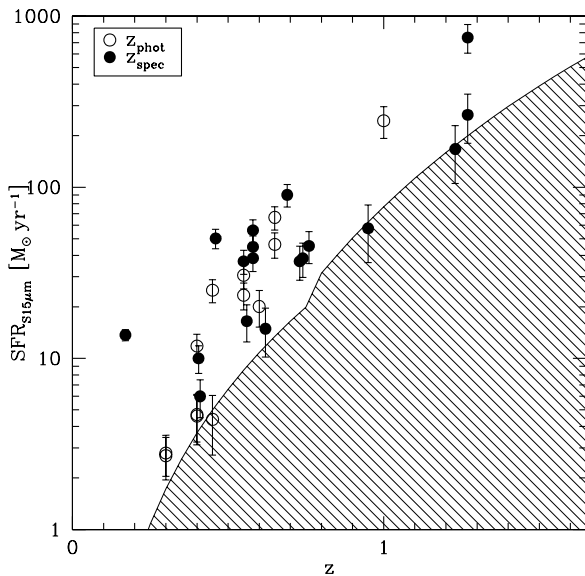


Fig. 5. Rates of star formation in the 15 μm sources based on the bolometric IR luminosity, as a function of redshift. Filled and open circles refer to objects with spectroscopic or photometric redshifts. The shaded area represents the unobservable region given by our sensitivity limit of 95 μJy imposed by the sample selection.

For the two other radio detections, S23 and S73, the radio and mid-IR fluxes are entirely consistent with a pure

starburst emission (see again Tables 6 and 7, and also Mann et al. 2002).

In summary, our analysis has found clear evidence for the presence of AGNs in two of the sample sources (the type-I S19, and the type-II S38). For a third source, S39, we suspect the presence of an AGN contribution because of morphology and a marginally broadened H_α line profile. For a fourth source, S82, the low LW3/LW2 flux ratio could indicate the contribution to the mid-IR spectrum of a type-II AGN. For all other HDF South sources any AGN contributions should be minor. Although the statistics is poor, this 10÷20% AGN fraction among the faint ISO sources is the same as found by Fadda et al. (2002) using the hard X-ray emission as AGN diagnostic. This is also in agreement with the results by Alexander et al. (2002) exploiting the 1 Msec Chandra X-ray exposure on the HDFN, in which 20 of the 41 ISOCAM sources were detected, 4 of which were classified as AGNs and 15 as emission line galaxies.

4.3. Estimating the Rate of ongoing Star Formation

Once the far-infrared activity of the source is reliably attributed to young stars, a fundamental indicator of the source physical status is the rate of ongoing star formation (SFR). Although UV-optical line and continuum emissions are contributed by newly born stars, Sanders & Mirabel (1996) have shown that starbursts with bolometric luminosities above $10^{10}L_\odot$ produce the bulk of their energy in the far-IR. For this reason, the bolometric IR luminosity of a starburst galaxy is the most direct and reliable estimator of star formation. It is then obviously important for us to compare our previous estimates of the SFR based on the H_α flux with more robust ones based on far-IR luminosities.

To this end, a measure of the source flux around 100 μm , where the galaxy IR SEDs are expected to peak, would be needed in principle. Unfortunately, this is not currently available to us in the HDF South. The imaging capabilities of ISO are strongly limited at such long wavelengths by the poor spatial resolution and high confusion noise (e.g. Franceschini et al. 2001). There is neither much perspective of an improvement until the operation of FIRST-Herschel in 2007. An important result by Elbaz et al. (2002), however, was to show that the mid-IR flux for a large variety of galaxies (from normal galaxies to luminous and ultra-luminous dusty starbursts) is extremely well correlated with the bolometric IR emission. They have shown that in a large sample of local objects only a very small fraction (\sim few %) show significant departures from this correlation (a remarkable such discrepant case is Arp 220, an ultra-luminous IR galaxy [ULIRG] showing a shortage of mid-IR flux compared with the far-IR one, due to dust self-absorption as evident from the PAH spectrum [Rigopoulou et al. 1999, Haas et al. 2001]).

This almost linear correlation of the bolometric far-IR and mid-IR luminosities was proven to hold in local

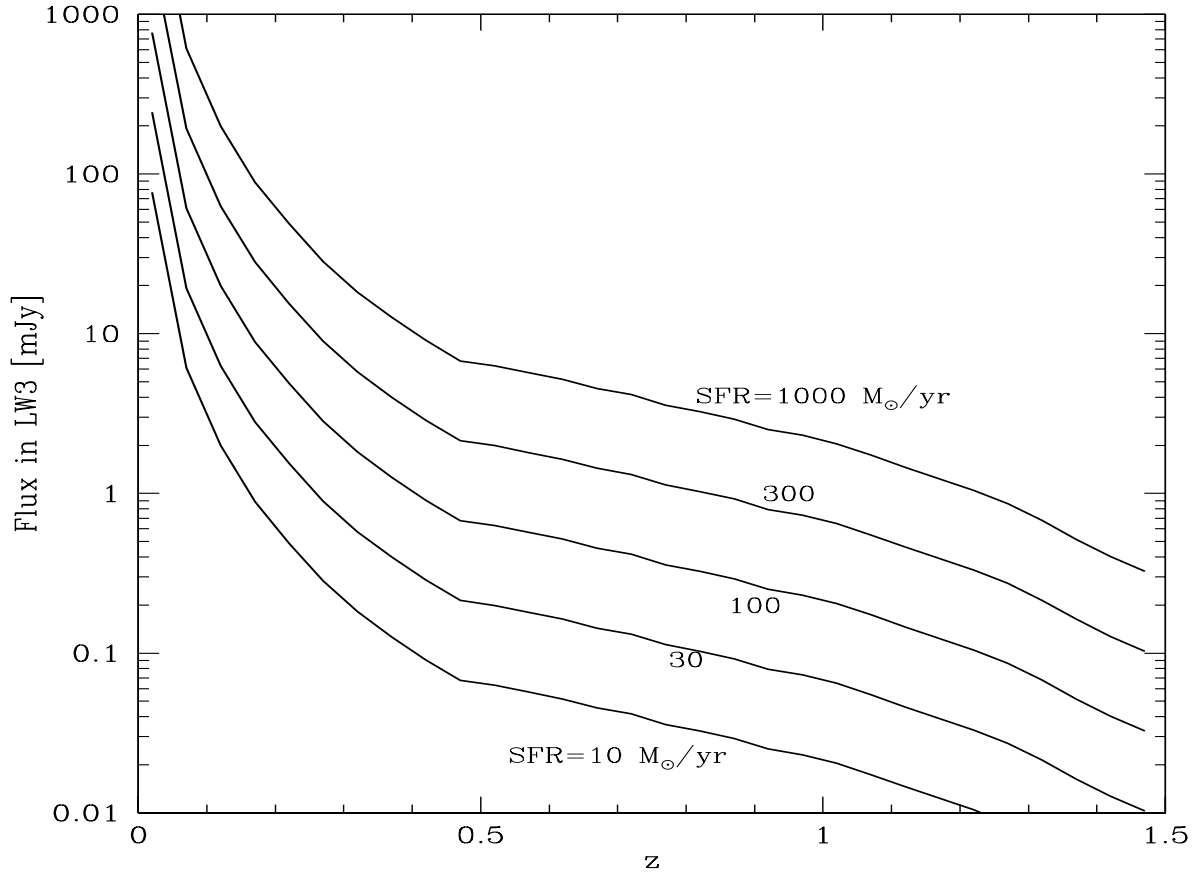


Fig. 6. Relation of the observed flux in the $15 \mu\text{m}$ LW3 ISO band versus redshift, as a function of the rate of star formation (SFR). This is based on the assumption that the IR flux is dominated by dust-reprocessed emission of young stars. The calibration of this relation has been obtained using the M82 spectral template, the detailed response function of the LW3 filter (see eqs. 5 and 7 in Franceschini et al. 2001) and the Kennicutt’s (1998) relation between SFR and L_{IR} for a Salpeter IMF between 0.1 and $100 M_{\odot}$.

galaxies by comparing the bolometric fluxes from IRAS data with mid-IR fluxes in various channels, including the IRAS $12 \mu\text{m}$ and the ISO LW3 and LW2 bands: considering that for sources at $z \sim 1$ the rest-frame emission in LW2 shifts to the observed LW3 band, this analysis by Elbaz et al. proved that the correlation is likely to hold for galaxies at least up to $z \sim 1$. This is also confirmed by the excellent match between the SFR estimates based on the mid-IR and radio fluxes for dusty starbursts at $z \leq 1$ (see Sect. 5.1 below, and Garrett 2002, Elbaz et al. 2002).

We applied the Elbaz et al. (2002) prescriptions to estimate the bolometric IR luminosity of our sources. At a redshift of $z > 0.8$ the LW3 band corresponds to the LW2 rest-frame, while for $z < 0.8$ the central wavelength of LW3 falls into the IRAS $12 \mu\text{m}$ filter. We therefore assumed that the luminosities computed from the LW3 fluxes of the sources in our sample originate from photons

emitted close to the LW2 and IRAS12 wavebands, and then used the Elbaz et al. relations:

$$\begin{aligned} L_{IR} &= 4.78^{+2.37}_{-1.59} \times (\nu L_{\nu}[6.75 \mu\text{m}])^{0.998} \\ &\quad \text{if } \nu L_{\nu}[6.75 \mu\text{m}] < 5 \times 10^9 L_{\odot} \\ &= 4.37^{+2.35}_{-2.13} \times 10^{-6} \times (\nu L_{\nu}[6.75 \mu\text{m}])^{1.62} \\ &\quad \text{if } \nu L_{\nu}[6.75 \mu\text{m}] \geq 5 \times 10^9 L_{\odot}, \end{aligned} \quad (3)$$

$$\nu L_{\nu}[15 \mu\text{m}] = 0.042 \times (\nu L_{\nu}[12 \mu\text{m}])^{1.12}, \quad (4)$$

$$L_{IR} \sim 11.1 \cdot \nu L_{\nu}[15 \mu\text{m}]. \quad (5)$$

From L_{IR} we then computed the SFRs adopting the Kennicutt’s (1998) calibration:

$$\frac{SFR}{M_{\odot} \text{yr}^{-1}} = 1.72 \cdot 10^{-10} L_{IR} [L_{\odot}]. \quad (6)$$

The results are reported in the fourth column of Table 6. Figure 5 shows a plot of these estimated SFRs as a function of redshift. The shaded area represents the unobservable region given by our sensitivity limit of $95 \mu\text{Jy}$ imposed by the sample selection. Error bars have been computed

on the basis of the 1σ uncertainties on the LW3 measurements only, while we did not take into account the scatters in the Elbaz’s and Kennicutt’s relations. The plot shows the effect of Malmquist bias induced by the $15\ \mu\text{m}$ flux limit of the sample, high redshift objects being detectable only if their luminosity, and SFR, are large enough.

We compare in Figures A.2 and A.3 the observed spectral energy distributions of our sample sources with the empirical SED of M82 scaled to fit the measured LW3 flux (thick continuous line). The M82 SED has been taken partly from Silva et al. (1998), partly from the observed ISOCAM–CVF low-resolution spectrum between 5 and $18\ \mu\text{m}$ by Foerster-Schreiber et al. (2001), in order to get a proper representation of the PAH spectrum which is critical for interpreting the LW3 fluxes. In the Elbaz’s et al. analysis this prototypical starburst falls close to the barycenter of the L_{FIR} to L_{15} correlation. The SFR values appearing in Figs. A.2 and A.3 refer to these fits, assuming for M82 a $SFR \simeq 6 M_{\odot} \text{yr}^{-1}$.

We report in Fig. 6 our estimated dependence of the SFR on the $15\ \mu\text{m}$ flux as measured in the ISOCAM LW3 filter, as a function of redshift, based on the M82 SED. This takes into account in detail the effects of the filter transmission function and the complex mid-IR spectrum in the K-correction factor. As discussed in Elbaz et al. (2002), values of the SFR based on the M82 template tend to be lower by $\sim 30 - 50\%$ than those based on the more sophisticated analysis based on Eqs. 3 to 6.

4.4. Estimating the baryonic masses

A second fundamental parameter characterizing the sources of the IR background, that we identified in the faint ISO galaxies, is their mass in stars. This integral of the past stellar formation activity in the galaxy provides a logical complement to the determination of the instantaneous rate of star formation. To measure galaxy masses in the HDF South, we have performed spatially-resolved medium-resolution spectroscopy with ISAAC of few selected targets. However, the long time integrations required have limited such dynamical estimates to 4 galaxies (see Rigopoulou et al. 2002).

A powerful alternative to the time-expensive spectroscopic investigations makes use of observations of the galaxy near-IR SEDs and their moderate dependence on the age of the contributing stars (e.g. Franceschini & Lonsdale, 2002). This is due to the fact that in a typical galaxy the stellar mass is dominated by low-mass stars, with evolutionary timescales of the order of the Hubble time. As discussed by several authors (Lancon et al. 1999, Origlia & Oliva 2000), these moderate-mass stars during the cool giant phase largely contribute to the near-IR SEDs of galaxies. However, dusty starbursts show occasional evidence in the starburst regions for the presence of younger red supergiants as shown by the pronounced [CO] $2.3\ \mu\text{m}$ absorption (e.g. Foerster-Schreiber et al. 2001). Obviously, a contribution by such young massive stars,

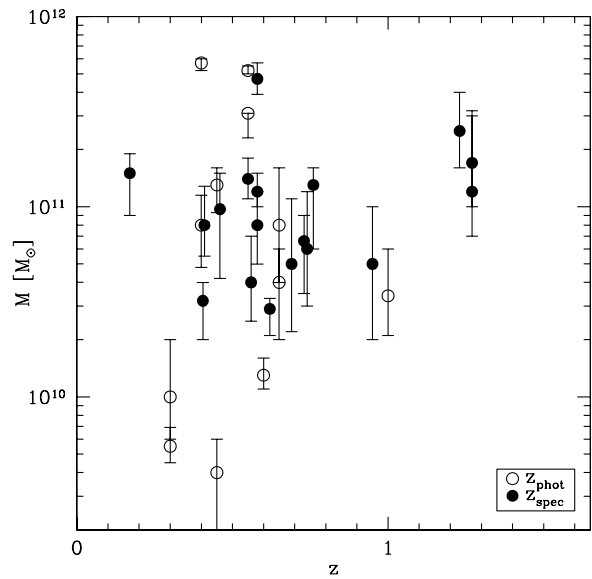


Fig. 7. Dependence of the masses estimated for the HDF–S $15\ \mu\text{m}$ sources on redshift z . Solid circles correspond to objects with spectroscopic and open circles with photometric redshifts.

even heavily extinguished, would substantially decrease the M/L in the near-IR, hence affecting the stellar mass estimate.

We have analysed the UV-optical-NIR data on our sample sources by means of a spectral synthesis code that we obtained from a modification of that described in Poggianti, Bressan & Franceschini (2001) and specifically devised to model dusty starbursting galaxies. The integrated model spectrum has been generated as a combination of 10 single stellar populations (SSP) of different ages: the youngest generations (10^6 , $3 \cdot 10^6$, $8 \cdot 10^6$, 10^7 yr) and the intermediate ($5 \cdot 10^7$, 10^8 , $3 \cdot 10^8$, $5 \cdot 10^8$, 10^9 yr), while the oldest populations of stars have been modelled as a constant star formation rate for $2 \cdot 10^9 < t < 12 \cdot 10^9$ yrs.

The composite spectrum of each SSP made use of the Padova isochrones with the Pickles (1998) spectra, also complemented with spectra from the Kurucz libraries (Bressan et al. 2001). Each stellar generation is born with a Salpeter IMF between 0.1 and $100 M_{\odot}$ and was assumed to be extinguished by dust in a uniform screen following the standard Galactic extinction law ($R_V = A_V/E[B - V] = 3.1$). The extinction value $E(B-V)$ was allowed to vary from one population to another, and the extinguished SSP spectra were added up to obtain the galaxy synthetic spectrum. Twenty parameters in total – i.e. the $E(B-V)$ and the stellar mass for each populations – are needed to define the synthetic spectrum. Note that such large number of independent stellar populations was used to get the best possible description of the observed spectra and conservative estimates of the uncertainties in the model parameters (namely the total stellar mass).

This completely free-form, non-parametric model was devised to account in the most general way for bursting and discontinuous star formation histories characteristic of starburst galaxies, as well as for more normal and quiescent formation patterns. It also provides easy implementation of different extinction properties for populations at different ages.

We have used this spectral synthesis code to perform an exploratory study of how degenerate are fits to the observed UV-optical-near-IR SEDs of IR starbursts against variations in the age and extinction of contributing stellar populations (Berta et al. 2002, in preparation). We have explored the model’s parameter space with the *Adaptive Simulated Annealing* method by Ingber (2000), including random-number generators, and using χ^2 as a goodness-of-fit test. Our simulations have shown that the age-extinction degeneracy seriously hamper the mass estimate, which may be uncertain by factors up to 5 or more for some dusty objects. This is partly because the optical-near-IR spectral continuum by itself leaves highly undetermined the contribution of supergiant stars to the near-IR flux.

To better constrain the incidence of young extinguished stellar populations and to evaluate their contribution to the galaxy’s M/L ratio, we have included in our spectral fitting procedure also the ISOCAM mid-IR LW3 flux, which is a good measure of the bolometric emission by young stars (see Sect. 4.3). To match the observed mid-IR flux, we have computed the far-IR spectrum associated with a given solution of our spectral synthesis model from the difference between the total non-extinguished and the total extinguished UV-optical-NIR flux, and assuming that this absorbed energy is re-radiated in the IR with the spectral shape of M82 (see Figs. A.2 and A.3). At the end, our observable set included the UV, optical, near-IR and mid-IR flux data for all sources, as reported in Figs. A.2 and A.3. Once a best-fitting solution was found, the total stellar mass in the galaxy was computed as the sum of the contributions by all stellar populations.

Our estimated values of the baryonic masses M and their uncertainties, as obtained with the above procedure, are reported in Table 6 (fifth and sixth columns) and plotted against redshift in Fig. 7. We see that, although we can exploit a good sampling of the galaxy SED, the uncertainties in the photometric mass estimates are still fairly large (typically a factor ~ 2). Given the very extensive exploration of the parameter space that we performed, we consider these as conservative estimates of the present uncertainties. Tighter constraints could soon be obtained from IRAC/SIRTF data between 3 and 10 μm over large sky areas, particularly from the SIRTF Legacy Programs GOODS and SWIRE (Dickinson 2002, Franceschini & Lonsdale, 2002).

The M values do not show significant correlation with z , e.g. compared with the strong observed correlation of SFR with z (Fig. 5). This reflects our primary selection not being on mass but on the SFR value, through the LW3 flux limit.

5. DISCUSSION

5.1. Comparison of independent SFR estimators

As expected given the nature of these sources selected for their strong mid-IR dust emission, the optical estimates of the SFRs based on H_α luminosities without extinction corrections provide values very significantly smaller than those obtained from the mid-IR flux [Fig. 8(a)]. Also the H_α -based and the IR-based SFR estimates are poorly correlated with each other.

A large scatter remains even after the H_α -based estimates are corrected for line-of-sight extinction, as illustrated in Figure 8(b) (open symbols here refer to A_V estimates based on fitting of the optical SEDs, filled symbols to estimates based on the Balmer line ratios).

Obj. #	z	ν GHz	S_ν μJy	L^\dagger (1.4 GHz)	SFR (1.4 GHz)
n 3	1.219	8.5	56.5	154.9	1093.00
n 7	0.078	8.5	17.5	0.104	0.74
n 17	0.556	8.5	10.2	4.520	31.89
n 20	0.961	8.5	190.0	299.4	2112.00 ²
n 28	0.410	8.5	26.0	5.711	40.29
n 32	1.275	8.5	15.1	45.84	323.40
s 19	1.57	4.9	163	542.0	3824.00 ²
s 19	"	8.5	111	547.2	3861.00 ²
s 23	0.46	1.4	200	14.99	105.80
s 23	"	2.5	149	14.92	105.30
s 23	"	4.9	127	17.81	125.70
s 39	1.27	1.4	109	92.70	654.00 ²
s 73	0.17	1.4	533	4.919	34.70
s 73	"	2.5	300	4.944	34.88

¹ Luminosities at 1.4 GHz in units of $10^{22} \text{ W Hz}^{-1}$.

² AGN objects: SFR is not a reliable estimate.

Table 7. Radio estimate of the SFR of 15 μm sources in both HDF’s and FF’s. In the first column objects named n are from the HDF–N sample, those with s in the HDF–S. The ISOCAM LW3 sources in HDF–N refer to the catalogue by Aussel et al. (1999). Third column specifies the frequency at which the fluxes in the fourth were measured. Data are from Richards (2000) and Mann et al. (2002).

An independent test of the SFR can be inferred from the radio flux: the radio emission is also unaffected by dust in the line-of-sight (though it might be sensitive in principle to free-free absorption at low radio frequencies for large column densities of ionized gas, and also sensitive to radio-loud AGN components). The relationship between the SFR and radio synchrotron emission is established by the number of type-II and type-Ib supernova explosions per unit time. Condon (1992) finds the relation

$$\frac{\text{SFR}(M > 5 M_\odot)}{M_\odot \text{yr}^{-1}} \simeq \frac{L_\nu(1.4 \text{ GHz})}{4 \cdot 10^{21} \text{ W Hz}^{-1}}. \quad (7)$$

For our adopted IMF, this becomes

$$\frac{\text{SFR}(M > 0.1 M_\odot)}{M_\odot \text{yr}^{-1}} \simeq \frac{L_\nu(1.4 \text{ GHz})}{1.2 \cdot 10^{21} \text{ W Hz}^{-1}}. \quad (8)$$

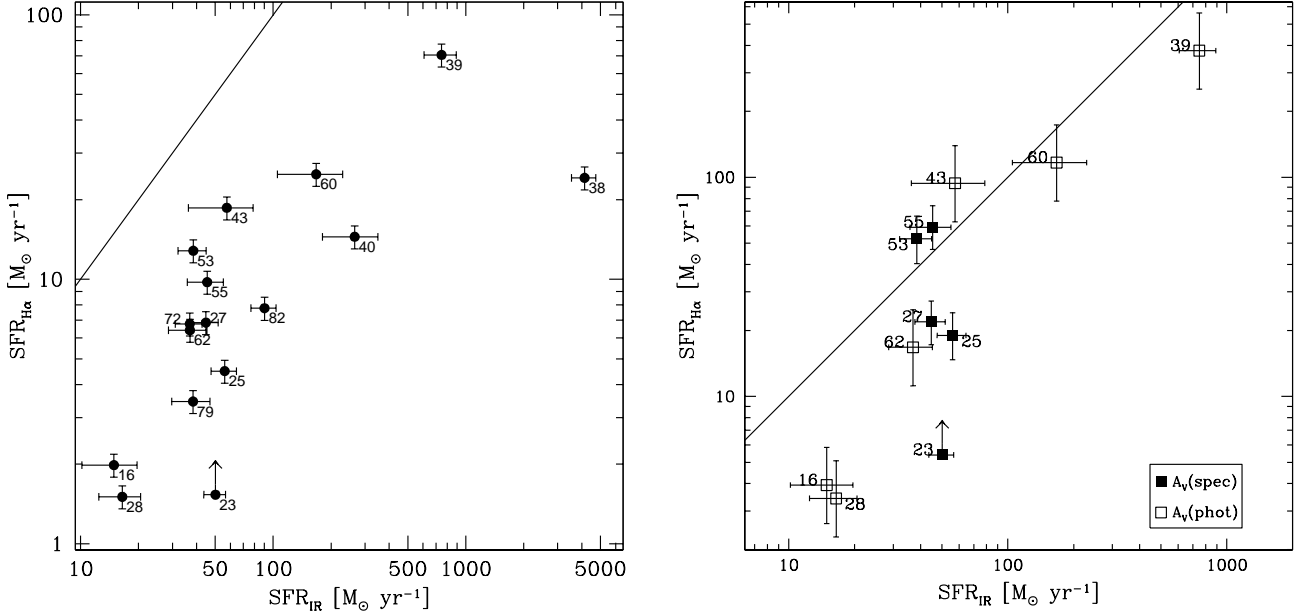


Fig. 8. Comparison between estimates of SFR based on the $H\alpha$ luminosity and those based on SED fitting of the mid-IR flux (as in Table 5). In panel (a) the $H\alpha$ flux is without extinction correction, in panel (b) it is corrected for extinction. Lines indicate the relation $SFR(H\alpha) = SFR(IR)$. In the right panel open squares refer to A_V estimates based on fits to the SED, and filled squares to extinction estimated from the Balmer line ratios. Error bars are based on flux uncertainties (propagating into the extinction estimate when $H\alpha$ is corrected).

To improve the statistics, we consider in this and the following sections source samples selected from deep ISO observations in both the HDF-S and the HDF-N. The ISOCAM LW3 datasets in both areas have been reduced in the same way. As for the HDF-N, the ISOCAM data reduction by Aussel et al. (1999) has detected 77 sources at $15\ \mu\text{m}$, 41 of which have $S_{15\mu\text{m}} > 100\ \mu\text{Jy}$ and constitute a complete sample over an area of 25 square arcmin (as for HDF-S). HDF-N sources with $S_{15\mu\text{m}} < 100\ \mu\text{Jy}$ do not form a complete sample, but they provide an useful extension covering the faint end of the galaxy luminosity function. All but 13 of the HDF-N sources have spectroscopic redshifts, while for the remaining we adopt the usual photometric estimate.

Then using published radio fluxes at 1.4, 2.5, 4.9 and 8.5 GHz for HDF-S galaxies by Mann et al. (2002) and for HDF-N by Richards et al. (1998) and Richards (2000), we computed the source luminosities at 1.4 GHz assuming for the radio emission a power-law with spectral index α_R , with $\alpha_R \simeq 0.7$ (the mean value for the HDF-N sample of Richards (2000)), except for sources S23 and S73, for which the spectral index turns out to be 0.5 and 1.0 respectively.

The SFR values found in this way, and reported in Table 7 and Fig. 9, are in good agreement with those based on the IR flux.

In both table and figure we report also the data for the sources *s19* and *n20* for which we found evidence for the presence of an AGN (*n20*, detected by *Chandra* in X-

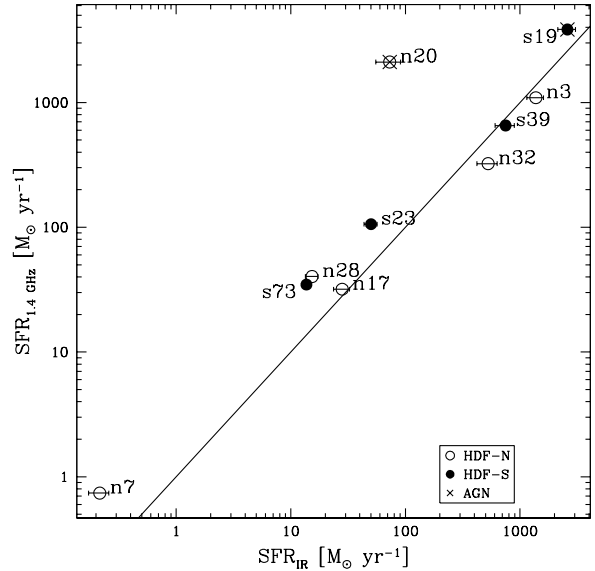


Fig. 9. Comparison between the estimates of SFR based on the radio flux and those inferred from fits to the mid-IR flux. The two methods provide consistent values in all cases where the radio is not contaminated by AGN emission (as is the case for the two crossed sources). Error bars on the IR estimate are based on the flux uncertainties only.

rays, is a recognized type-I AGN, see Hornschemeier et al. (2001); Brandt et al. (2001)): a comparison of the radio-

based SFR value with those reported in Table 6 provides an interesting test of an AGN contribution. The good match of SFR values based on the radio and the IR confirms the reliability of the latter as a SFR estimator (see also Elbaz et al. 2002, Garrett 2002).

The rates of SF indicated by our analysis for the faint ISO sources at $z > 0.5$ range from few tens to few hundreds solar masses/yr, i.e. a substantial factor larger than found for faint optically-selected galaxies.

Altogether, our analysis confirms that the mid-IR light is a good tracer of the star-formation rate, since it correlates well with the radio and H_α line fluxes (Figs. 8b and 9). On the other end, even after correcting for dust extinction, SFR estimates based on the H_α line flux underestimate the intrinsic SFR of luminous IR galaxies by a factor ~ 2 , with some large scatter. We have to consider, however, that large and uncertain correction factors have been applied due to the poor spatial sampling and dust extinction effects on the H_α measurement, which might explain it. Arguments in favour of a large intrinsic scatter between optical line and IR bolometric fluxes were discussed e.g. in Cram et al. (1998), Poggianti & Wu (2000), Rigopoulou et al. (2000), Poggianti et al. (2001), see also Goldader et al. (2002).

This issue will be possibly solved only with the advent of the new-generation of optical and near-IR Integral Field Spectrographs on large telescopes (e.g. VIMOS and SPIFFI/SINFONI on the ESO VLT, see Thatte et al. 1998), providing data of high spatial resolution and sensitivity on the optical-UV emissions in such morphologically complex systems.

5.2. Timescales for star formation

A proper characterization of the evolutionary status of the faint ISO source population and their relevance for the general process of galaxy formation comes from matching the rate of ongoing star-formation SFR with the mass of already formed stars. Such comparison is essentially independent of the stellar IMF (the same scaling factor would apply to both SFR and M by changing the IMF).

We report in Figure 10(a) the ratio of the baryonic mass to the SFR against redshift for ISO sources in HDF-S and HDF-N. For all these we determined masses and SFRs as discussed in Sect. 4.4. This *activity parameter*, $t_{SF}[yr] = \frac{M}{SFR}$, is a measure of the timescale for the formation of stars. The figure shows that, on top of a very large scatter, there is an apparent trend for the SF timescale t_{SF} to decrease with z (the Spearman rank coefficient is $\rho = -0.44$ for the whole sample of 109 sources, with a very significant correlation probability [$> 99\%$]).

On one side, this result indicates that galaxies at $z \simeq 1$ and larger are more actively forming stars than those in the local universe: a lower t_{SF} suggests that the ongoing SF is more significantly contributing to the observed stellar mass, and a larger fraction of stars are being formed during the current SF event. Of course, we expect a se-

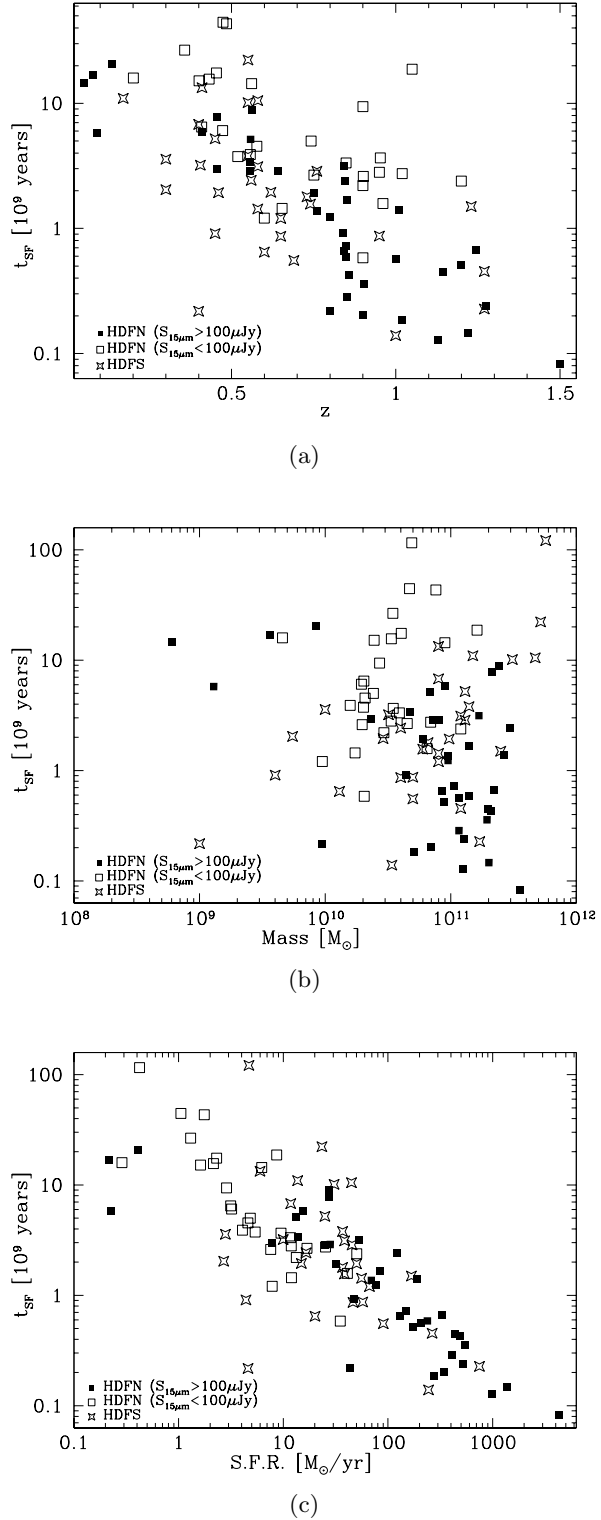


Fig. 10. The timescale of star formation $t_{SF} = M/SFR [10^9 \text{ yrs}]$ of faint ISO sources as a function of redshift (panel a), mass in stars (panel b) and SFR (panel c).

lection effect to play, if we consider that at the higher redshifts only the IR brightest galaxies can be detected

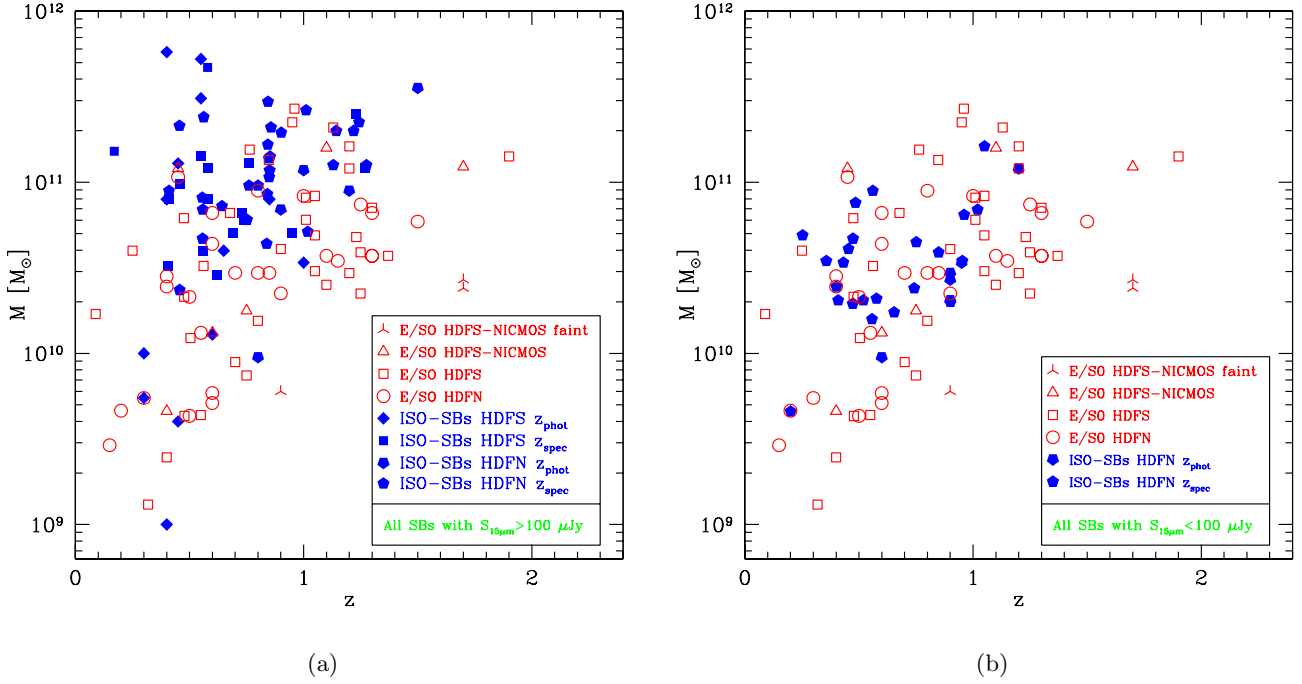


Fig. 11. Comparison of the masses determined for the $15 \mu\text{m}$ sources in both HDF, with those of normal elliptical/S0 by Rodighiero et al. (2001). Panel (a) regards the ISO objects with $S_{15\mu\text{m}} > 100 \mu\text{Jy}$, (b) those fainter. See text for comments.

in the flux-limited samples, while the selection is less directly influenced by the stellar mass. We expect that our main selection bias should operate in preventing detection of sources in the upper right corner of Fig. 10(a): less active galaxies, those with the highest t_{SF} at the higher redshifts, are not detected at $15 \mu\text{m}$ due to our limited sensitivity.

On the contrary, we do not expect that sources are missed in the other corner at lower t_{SF} (lower left side in the figure). One effect to consider here is the low redshift of the sources and the small sampled volume: although detecting a luminous massive galaxy becomes less likely here, luminosities and masses suffer a similar bias, so the net effect on t_{SF} should be negligible.

Figures 10(b) and 10(c) plot the star-formation timescale against the stellar mass and the SFR. The former shows that there is essentially no dependence of t_{SF} on M . Some clear segregation is evident in both Figs. 10(b) and 10(c) between sources brighter and fainter than $S_{15} = 100 \mu\text{Jy}$: the latter are systematically shifted towards lower values of the mass and SFR, and to higher values of t_{SF} (if we exclude a few low-redshift and low-mass galaxies). Apparently, the fainter $15 \mu\text{m}$ sources correspond to a less "active" class, closer to the quiescent spiral galaxy population.

Altogether, our analysis indicates a trend for a decreased activity of star-formation (per unit stellar mass) in galaxies at lower redshifts.

5.3. Comparison with normal galaxies selected in the K band

We gain further insight into the nature of the $15\mu\text{m}$ -selected population from a match with galaxy samples selected in the optical or near-IR. We compare here the baryonic masses, while we do not consider the SFRs whose estimate based on optical data may be quite uncertain. Figures 11 and 12 compare the distributions of stellar masses versus redshift for the IR-selected sources with those of K -band selected galaxies with morphological classification in the HDF-N and HDF-S (filled symbols refer to the ISO galaxies, open symbols to the K -selected galaxies). In Fig. 11 the reference sample are 69 morphologically-classified E/S0 galaxies with $K < 20.15$ in the WFPC-2 HDF-N and HDF-S (plus a few NICMOS-HDFS sources), over a total area of 11.7 arcmin^2 (Rodighiero et al., 2001).

The comparison in Fig. 12 is performed with a sample of 52 morphologically classified spiral/irregulars with $K < 20.47$ in the 5.7 arcmin^2 WFPC-2 HDF-N field (Rodighiero et al., 2000). For all datasets, the baryonic masses are consistently estimated from fits to the optical/near-IR SEDs, as discussed in Sect. 4.4 (previous results by Rodighiero et al. have been corrected for consistency with our assumed cosmology). Panels (a) and (b) in both figures concern the bright ($S_{15\mu\text{m}} > 100 \mu\text{Jy}$) and faint ($S_{15\mu\text{m}} < 100 \mu\text{Jy}$) $15 \mu\text{m}$ subsamples respectively. These figures provide evidence that the IR-selected sources include a population of rather massive galaxies

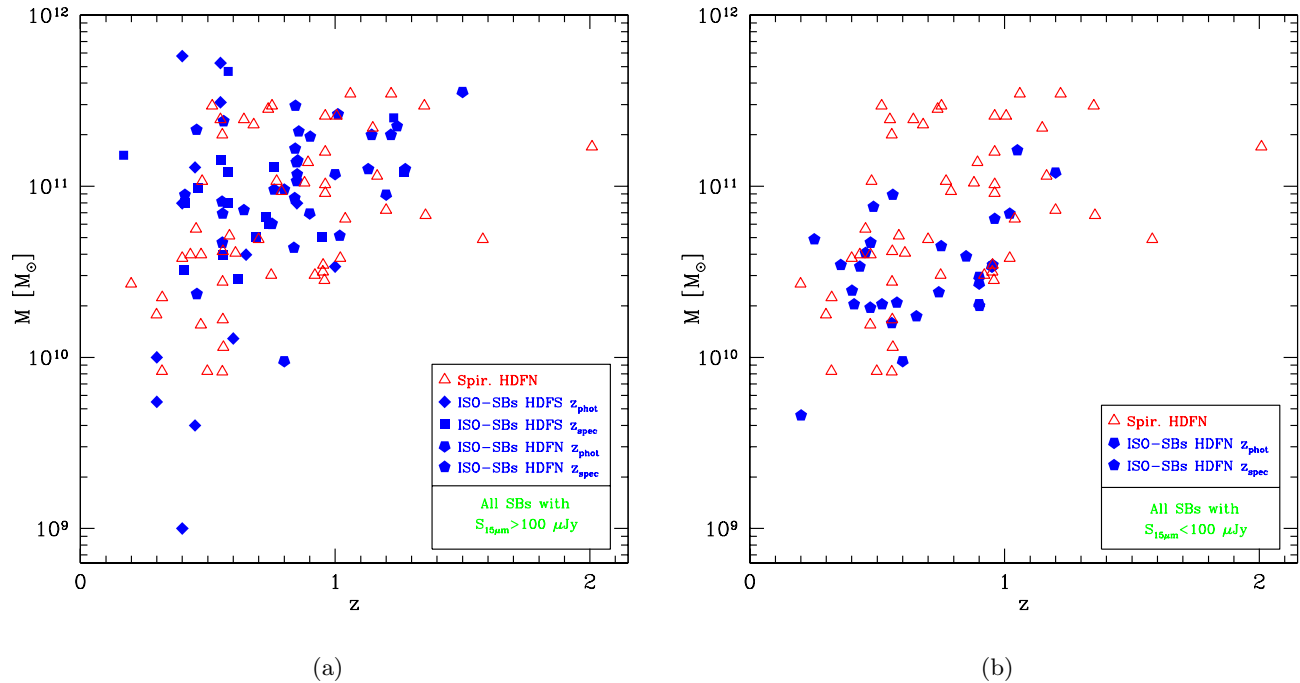


Fig. 12. Comparison between the baryonic masses in stars for the counterparts to the LW3 sources (filled symbols) and those of normal spirals and irregulars in Rodighiero et al. (2000) (open symbols). Panel (a): ISO sources with $S_{15\mu m} > 100\mu Jy$. Panel (b): sources with $S_{15\mu m} < 100\mu Jy$. The meaning of the different symbols are mentioned in the figure insets.

when compared with those selected in K, (particularly if we consider that, for reasons mentioned in Sect. 4.4, the K-flux limit is expected to select the most massive objects). This is particularly apparent among the IR brighter subsample (see panels [a]), whose mass distribution shows a tendency to occupy a region of high mass values compared with K-band selected E/S0 galaxies. Fainter $15\mu m$ sources (panels [b]) appear to be hosted by more moderately massive systems.

Note that, in any case, this comparison of IR-selected and K-band selected galaxies has to be taken with some care due to the different sizes of the fields covered by the ISO surveys ($\sim 50 arcmin^2$) and by the near-IR samples (5 to 10 $arcmin^2$). These latter are particularly subject to variance effects due to the small sampled volumes. The ISO samples themselves show evidence of conspicuous structure: two overdensities or clusters are evident in Figs. 11 and 12 at $z \simeq 0.58$ for LW3 sources in HDF-S and at $z \simeq 0.84$ in the HDF-N: associated with these we can notice galactic mass distributions spread towards high values. Mann et al. (2002) report a detailed discussion of the cosmic variance and sampling effects in the HDF-S.

5.4. Nature of the IR-selected galaxy population

It is evident from the previous discussion that the ISO surveys above $100\mu Jy$ select a population of massive galaxies which are associated with active sites of star formation. The WFPC-2 images show clear evidence for inter-

actions and mergers in $\sim 50\%$ of these galaxies (Berta, 2000; see also Fig. A.2). The redshift survey in the HDF-N by Cohen et al. (1999) has also revealed that the LW3 sources are almost invariably associated with peaks in the sample redshift distribution, which may be interpreted as either "walls" in the galaxy large scale structure, or galaxy groups. In such environment galaxy interactions are maximally efficient.

How much of these large stellar masses are formed during the ongoing event of star formation identified by the excess mid-IR emission? Are the currently observed episodes of star formation responsible for the bulk of the stellar content? Hints can be inferred from the star-formation timescales reported in Fig. 10. Values of the *activity parameter* t_{SF} here show a large scatter and rather uniform distribution between those characteristic of inactive galaxies ($t_{SF} \sim 10^{10} yrs$) and those of very active starbursts with $t_{SF} < 10^9 yrs$. The observed median value $t_{SF} \sim 1$ Gyr, compared with typical starburst timescales of ~ 0.1 Gyr, implies that *a single starburst event may explain only a fraction of the whole stellar content. A few to several such episodes are then required to build up the observed large galactic masses, as part of a protracted SF history made of a sequence of starbursting episodes on top of a lower-level secular SF.*

Another interesting fact illustrated in Fig. 10(a) is that the parameter t_{SF} expressing the "activity stage" of the ISO sources is rather uniformly distributed between values corresponding to *maximal* activity ($t_{SF} \leq 10^9 yrs$) and

those corresponding to almost inactive systems ($t_{SF} \geq 10^{10} \text{ yrs}$). This implies that in between the levels of *maximal* and *minimal* activity there is a continuity of intermediate stages.

In conclusion, the mid-IR flux efficiently discriminates distant IR galaxies as for not only their "activity level" (t_{SF}^{-1}), but also for the absolute values of the stellar mass and SFR: the brighter ($S_{15} > 100 \mu Jy$) IR-selected sources appear to be more extreme in any sense, typically more massive, more luminous, and with higher SFR. This star formation is likely triggered by strong dynamical interactions and mergers among the brightest members of galaxy groups. High SFRs and already large M values imply that these are presumably the formation sites of the most massive current-day galaxies.

6. Conclusions

We have investigated the characters of IR emissions in galaxies over a fair cosmic volume between $z \sim 0.2$ and 1.5. In particular, we have systematically exploited the mid-IR flux as a best and most reliable tracer of star-formation. This study makes use of combined observations with the *Infrared Space Observatory* and ESO VLT of faint mid-IR sources selected with the ISOCAM broad-band filter between 12 and 18 μm down to $S_{15} \sim 100 \mu Jy$ and below.

Previous analyses by Elbaz et al. (2002) and Franceschini et al. (2001) have shown that, given their areal densities, redshifts, and far-IR spectra, these faint sources are very likely responsible for an important fraction (of the order of 50%) of the energy density contained in the Cosmic IR Background between 10 and 1000 μm . In consideration of the fact that the CIRB is the major radiant component in the universe after the CMB and that it involves more energy than the UV, optical, and X-ray backgrounds put together, we expect that these objects have played an important role in the process of galaxy formation.

We have reported on low-resolution spectroscopic observations with the near-infrared ISAAC and optical FORS spectrographs on VLT for a representative and unbiased subsample of 21 objects selected in HDF-S. In addition to data on line-emissions and the mid-IR fluxes at 15 and 7 μm , we have made use of the rich variety of photometric observations in the UV-optical and near-IR to derive further constraints on the physics of the sources. To improve the statistics, we have also used in our analysis a sample of mid-IR sources at similar depths in the HDF-N observed by Aussel et al. (1999).

Our main conclusions are hereby summarized.

- Fairly intense $H_{\alpha} + [NII]$ emission is detected in virtually all the observed sources. The comparison with the H_{β} and $[OII]$, as well as the SED's analysis, indicate typically high extinction values $A_V \sim 1.5 - 2$ to affect the line ratios, quite larger than found for local normal spirals. While obviously coherent with the IR-selection emphasizing excess dust emission, this shows that the

intrinsic (de-reddened) H_{α} flux is strong in these objects. Enhanced activity is also proven by the fact that the mid-IR flux is typically larger by factors $> 2 - 3$ than expected for normal galaxies.

- We have investigated evidence for the presence of Active Galactic Nuclei in the core sample of 21 sources, as possibly responsible for such enhanced activity, by combining all available information: the broadness of the Balmer lines, the morphology of the optical counterparts from the WFPC-2 images, the shape of the mid-IR spectrum (from the LW3/LW2 flux ratio), and the ratio of the radio to IR flux. We have found uncontroversial evidence for nuclear activity in only 2 objects (S19, a type-I quasar at $z=1.57$, and S38, a luminous type-II AGN at $z=1.39$), while for two other objects (S39, a very luminous ULIRG at $z=1.27$, and S82 at $z=0.69$) we suspect the presence of AGN contributions. Although the statistics is poor, this result showing a low AGN fraction $\simeq 10 - 20\%$ among the faint IR sources is entirely consistent with that found by Fadda et al. (2002) based on deep hard X-ray data.
- Then assuming that for the bulk of these objects a starburst is the dominant energy source, we estimated the rates of star-formation SFR from all available indicators (H_{α} line flux, mid-IR and radio emissions). We confirm that the mid-IR light is a good tracer of the star-formation rate, since it correlates well with the radio and H_{α} line fluxes (Figs. 8b and 9). We found typically high values of $SFR \sim 10 - 300 M_{\odot}/yr$ for our IR-selected galaxies. On the other hand, even after correcting for dust extinction, SFR estimates based on the H_{α} line show a large scatter and some systematic offset compared with the intrinsic SFR of luminous IR galaxies. It still remains to be checked with sensitive IR Integral Field spectrographs whether this is due to poor spatial sampling by the slit spectrograph, or to an intrinsic depletion of the optical emission by large dust extinction in the SF regions of the most active starbursts.
- We have exploited the excellent coverage of the SED in the optical/near-IR to estimate the second fundamental parameter, the mass in stars M, by making use of a newly-devised tool to quantify the M/L of stellar populations with different ages and extinction. We find that the faint IR sources with fluxes $S_{15} > 100 \mu Jy$ are hosted by massive galaxies ($M \simeq 10^{11} M_{\odot}$), even if compared with those selected in the K band at similar redshifts. Spatially-resolved near-IR spectroscopy of a few of these galaxies by Rigopoulou et al. (2002) supports this result.
- By matching these large stellar masses with the observed rates of SF, we have determined timescales for SF of $t_{SF} \sim 0.2$ to 10 Gyrs. When compared with the t_{SF} values ($\sim 10^8 \text{ yrs}$) typically found for starbursts, this implies that the ongoing SF can generate only a fraction of the stellar content in these galaxies, many of such repeated episodes during a protracted SF history being required for the whole galactic build-up. A

trend towards a reduced level of star-formation activity in galaxies at decreasing redshift is also apparent in our data.

In summary, the 15 μm selection appears to emphasize sites of enhanced star formation inside massive galaxies, which are typically the brightest members of galaxy groups. These sources probably trace evolutionary phases, involving strong dynamical interactions and mergers, bringing to the formation of massive current-day galaxies.

Acknowledgements. We thank N. Thatte for support during the ISAAC 2001 run. This research has been supported by the Italian Space Agency (ASI) and the European Community RTN Network "POE", under contract HPRN-CT-2000-00138.

References

- Alexander, D.M., Aussel, H., Bauer, F.E., brandt, W.N., Hornschemeier, A.E., Vignali, C., Garmire, G.P. & Schneider, D.P.: 2002, *ApJ*, **568**, L85.
- Altieri, Metcalfe, L., Kneib, J.P., et al: 1999, *A&A*, **343**,.
- Appenzeller, I., et al.: 2000, *The ESO Messenger*, Vol. 100, 44.
- Aussel, H., Cesarsky, C. J., Elbaz, D. & Stark, J. L.: 1999, *A&A*, **342**, 313.
- Aussel, H. et al.: 2003, in preparation
- Baldwin, J. A. & Stone, R. P. S.: 1984, *MNRAS*, **206**, 241.
- Barger, A. J., Cowie, L.L., Sanders, D. B. Fulton, E., Taniguchi, Y., Sato, T., Kawara, K. & Okuda, H.: 1998, *Nature*, **394**, 248.
- Blain, A. W., Kneib, J.-P., Ivison, R. J., Smail, I., 1999, *ApJ* 512, L87.
- Berta, S.: 2000, Degree Thesis, Padova University.
- Brandt, W. N., Hornschemeier, A. E., Alexander, D. M., Garmire, G. P., Schneider, D. P., Boos, P.S., Townsley, L. K., Bautz, M. W., Feigelson, E. D. & Griffiths, R. E.: 2001, *AJ*, 122, 2810.
- Bressan, A., Poggianti, B., Franceschini, A., 2001, in "QSO hosts and their environments", Isabel Mrquez, Josefa Masegosa, Ascencion Del Olmo, Lucas Lara, Emilio Garca, and Josefina Molina Eds., Academic / Plenum Publishers, 171
- Chapman, S.C., et al., 2000, *MNRAS* 319, 318.
- Cohen, J., et al., 2000, *ApJ* 538, 29.
- Coleman et al.: 1980, *ApJS*, 43, 393.
- Condon, J. J.: 1992, *ARA&A*, **30**, 575.
- Cram, L., Hopkins, A., Mobasher, B., Rowan-Robinson, M.: 1998, *ApJ*, 507, 155.
- Da Costa et al.: 1998, *A&A* submitted, astro-ph/9812105.
- Devillard, N.: 1998, *Messenger*, 87, 19.
- Dickinson, M., 2002, to appear in the Proceedings of the ESO Workshop "The Mass of Galaxies at Low and High Redshift", R. Bender and A. Renzini Eds., Springer-Verlag Series "ESO Astrophysics Symposia".
- D'Odorico, S.: 1990, *The Messenger* 61, 51.
- Elbaz, D., Cesarsky, C. J., Fadda, D., Aussel, H., Desert, F.-X., Franceschini, A., Flores, H., Harwit, M., Puget, J.-L., Starck, J. L., Clemens, D., Danese, L., Koo, D. C. & Mandolesi, R.: 1999, *A&A Letters*, 351, 37L.
- Elbaz, D., Cesarsky, C., Chanical, P., Aussel, H., Franceschini, A., Fadda, D. & Chary, R.: 2002, *A&A* 384, 848.
- Ellis, R. S.: 1997, *ARA&A*, 35, 389.
- Fadda, D., Flores, H., Hasinger, G., Franceschini, A., Altieri, B., Cesarsky, C. J., Elbaz, D., Ferrando, Ph.: 2002, *A&A* 383, 838.
- Fioc, M. and Rocca-Volmerange, B.: 1997, *A&A*, 326, 950.
- Fitzpatrick: 1999, *PASP*, **111**, 63.
- Foerster-Schreiber, N. M. F., Genzel, R., Lutz, D. Kunze, D. & Sternberg, A.: 2001, *ApJ*, 552, 544.
- Fomalont, E. B., Windhorst, R. A., Kristain, J. A. & Kellermann, K. I.: 1991, *AJ*, 102, 1258.
- Franceschini A., Fadda D., Cesarsky C.J., Elbaz D., Flores, H., Granato, G.L.: 2002, *ApJ* 568, 470
- Franceschini A., Aussel H., Cesarsky C., Elbaz D., Fadda D.: *A&A*, 2001, 378, 1.
- Franceschini, A.: 2001, Proceedings of the Workshop "Starburst Galaxies. Near and Far", L. Tacconi and D. Lutz Eds., Springer-Verlag
- Franceschini, A., & Lonsdale, C.: 2002, To appear in the Proceedings of the ESO Workshop "The Mass of Galaxies at Low and High Redshift", R. Bender and A. Renzini Eds., Springer-Verlag Series "ESO Astrophysics Symposia" (astro-ph/0202463)
- Garrett, M. A.: 2002, *A&A* 384, L19
- Genzel, R. et al.: 1998, *ApJ*, **498**, 579.
- Genzel, R., & Cesarsky, C.J., 2000, *ARAA* 38, 761.
- Goldader, J., Meurer, G., Heckman, T., et al., 2002, *ApJ*, **568**, 651.
- Granato. G.L., Danese, L., Franceschini, A., 1997, *ApJ*, **486**, 147.
- Ingber, L., 2000, <http://www.ingber.com>
- Haas et al. 2001 *AA* 367, L9
- Helou, G., Soifer, B.T., Rowan-Robinson, M., 1985, *ApJ* 298, L7
- Hook, R.: 1999, *ST-ECF Newsletter*, **26**, 1.
- Hornschemeier, A. E., Brandt, W. N., Garmire, G. P., Schneider, D. P., Barger, A. J., Broos, P. S., Cowie, L. L., Townsley, L. K., Bautz, M. W., Burrows, D. N., Chartas, G., Feigelson, E. D., Griffiths, R., Lumb, D., Nousek, J. A., Ramsey, L. W. & Sargent, W. L. W.: 2001, *ApJ* 554, 742.
- Hughes, D., Hughes, D. H., Serjeant, S., Dunlop, J., Rowan-Robinson, M., Blain, A., Mann, R. G., Ivison, I., Peacock, J., Efstathiou, A., Gear, W., Oliver, S., Lawrence, A., Longair, M., Goldschmidt, P. & Jenness, T.: 1998, *Nature*, **394**, 241.
- Hummer, D. G. & Storey, P. J.: 1987, *MNRAS*, **224**, 801.
- Kennicutt, R. C.: 1998, *ARA&A*, **36**, 189.
- Lancon, A., Mouhcine, M., Fioc, M., Silva, D.: 1999 *A&A* 344, L21.
- Leitherer, C. et al.: 1999, *ApJS*, **123**, 3L.
- Lutz, D., Spoon, H. W. W., Rigopoulou, D., Moorwood, A. F. M., Genzel, R., 1998, *ApJ* 505, L103.

- Mann, R. G., Oliver S., Carball, R., Franceschini, A., Rowan-Robinson, M., Heavens, A. F., Kontizas, M., Elbaz, D., Dapergolas, A., Kontizas, E. E., Granato, G. L., Silva, L., Rigopoulou, D., Gonzalez-Serrano, J. I., Verma, A., Serjeant, S., Efstathiou, A. & Van der Werf, P. P.: 2002, *MNRAS* 332, 549.
- Moorwood, A.F.M., et al., 1998, *Msngr* 74, 7.
- Okumura, K.: 1998, *ESA ISOCAM PSF Report*.
- Oliver, S. et al.: 1997, *MNRAS*, **289**, 471.
- Oliver, S. et al.: 2000, *MNRAS*, **316**, 749.
- Oliver, S. et al.: 2002, *MNRAS* 332, 536.
- Origlia, L., Oliva, E.: 2000, *A&A* 357, 61.
- Pei, Y.C.: 1992, *ApJ*, **395**, 130.
- Pickles, A.: 1998, *PASP*, **110**, 863.
- Poggianti, B. & Wu, H.: 2000, *ApJ*, **529**, 157.
- Poggianti, B., Bressan, A., Franceschini, A., 2001, *ApJ* 550, 195.
- Poggianti, B.: 1997, *A&AS*, **122**, 399.
- Puget, J.-L., Abergel, A., Bernerd, J.-P., Boulanger, F., Burton, W. B., Desert, F.-X. & Hartmann, D.: 1996, *A&A*, **308**, L5.
- Richards, E. A., Kellermann, K. I., Fomalont, E. B., Windhorst, R. A. & Partridge, R. B: 1998, *AJ*, **116**, 1039.
- Richards, E. A.: 2000, *AJ*, **533**, 611.
- Rigopoulou, D., Spoon, H. W. W., Genzel, R., Lutz, D., Moorwood, A. F. M., Tran, Q. D.: 1999, *AJ* 118, 2625.
- Rigopoulou, D., Franceschini, A., Aussel, H., Genzel, R., Van den Werf, P., Cesarsky, C. J., Dennefeld, M., Oliver, S., Rowan-Robinson, M., Mann, R. G., Perez-Fournon, I. & Rocca-Volmerange, B.: 2000, *ApJ*, **537**, L85.
- Rigopoulou, D., Franceschini, A., Aussel, H., Genzel, R., Thatte, N., Cesarsky, C. J.: 2002, *ApJ* 580, 789.
- Rodighiero, G., Granato, G. L., Franceschini, A., Fasano, G. & Silva, L.: 2000, *A&A*, **364**, 517.
- Rodighiero, G., Franceschini, A. & Fasano, G.: 2001, *MNRAS*, **324**, 491.
- Rowan-Robinson et al.: 1997, *MNRAS*, **289**, 490.
- Rowan-Robinson, M.: 2000, *ApJ*, 549, 745.
- Rudnick, G., Franx, M., Rix, H.W., et al.: 2001, *AJ*, 122, 2205.
- Sanders, D. & Mirabel, I. F.: 1996, *ARA&A*, **34**, 749.
- Silva, L., Granato, G. L., Bressan, A. & Danese, L.: 1998, *ApJ*, **509**, 103.
- Stark, J.L., Aussel, H., Elbaz, D., Fadda, D. & Cesarsky, C. J.: 1999, *A&AS*, **138**, 365.
- Sternberg, A.: 1998, *ApJ*, **506**, 721.
- Stone, R. P. S. & Baldwin, J. A.: 1983, *MNRAS*, **204**, 347.
- Thatte, N.A., Tecza, M., Eisenhauer, F.: 1998, *SPIE* 3353, 704.
- Teplitz, H. I., Gardner, J. P., Palunas, P., Sahu, M. S., Malumuth, E. M., Woodgate, B. E., Heap, S. R., Williger, G. M., Danks, A. C., Smette, A., Brown, T. M., Kaiser M. E. & Gull, T. R.: 1998, in *American Astronomical Society Meeting*, **193**, 7507.
- Tran, Q.D., Lutz, D., Genzel, R., et al.: 2001, *ApJ* 552, 527.
- Sanders, D., & Mirabel, I.F.: 1996, *ARAA* 34, 749.
- Smail, I., Ivison, R. & Blain, A. W.: 1997, *ApJ Letters*, **490**, L5.
- Tresse, L., Dennefeld, M., Petitjean, P., Cristiani, S. & White, S.: 1999, *A&A Letters*, **346**, L21.
- Thornley, M. D., Foerster-Schreiber, N. M., Lutz, D., Genzel, R., Spoon, H.W.W. & Kunze, D: 2000, *ApJ*, **539**, 641.
- van der Blik, N.S., Manfroid, J. & Bouchet, P.: 1996, *AAPS*, **119**, 547.

Appendix A: Notes on individual sources

Some properties of individual sources are hereby summarized. Imaging data and SEDs mentioned here refer to those of Figs. A.2. Images are from the HDF South WFPC-2 V-606 band observations.

S14. Outside the area covered by WFPC-2, the [OII], H_β and [OIII] lines have been detected with EMMI at $z=0.41$. The optical spectrum is quite bluer than that of M51, and is fit by the SED of a massive, moderately star-forming spiral with $SFR=16.5 M_\odot yr^{-1}$, as also revealed by the modest excess of the LW3 15 μm flux above the M51 spectrum.

S16. Also outside the HST fields, it shares very similar properties to S14, with an H_α detection at $z=0.62$.

S19 is an WFPC-2 point-like source, detected also at 4.9 and 8.5 GHz Mann et al. (2002). Its SED (Fig. A.2) is virtually a flat power-law from 0.3 to 20 μm . The ISAAC spectrum reveals a strongly broadened (FWHM $\sim 260 \text{ \AA}$) H_α at $z=1.57$. The corresponding velocity field ($\Delta v > 4600 \text{ km/s}$) indicates this source to be a type-I quasar. Two broad emission features are also detected in the FORS spectrum of Fig. 4(d), corresponding to $MgII\lambda 2798$ and $CIII]\lambda 1908$ at redshift $z \simeq 1.56$. The observed SED is reproduced by a combination of a starburst template in the optical and a type I AGN model. The latter is taken from Granato, Danese & Franceschini (1997) and Franceschini et al. (2002), with best-fit parameters $R = 300$ (ratio between inner and outer tori radii) and equatorial optical depth $\tau_\nu = 50 \text{ mag}$ at 0.3 μm .

S20. Very similar to S14 and S16 in all respects, two lines detected by EMMI are [OII] and H_β at $z=0.39$. The overall SED is quite well fit by the M51 template, and the source looks like a massive but relatively normal and quiescent ($SFR = 11 M_\odot yr^{-1}$) spiral galaxy.

S23 has been observed with NTT/EMMI, FORS2 and ISAAC on VLT (ISAAC observations are from Rigopoulou et al. 2000). It appears as a triple system in the HST image, but unfortunately only one of the three nuclei (that in the middle) has been included in the spectrograph slits because of the limited orientation capabilities. Four emission lines are detected at redshift $z=0.46$. The central source in the triplet, which we identify as that mostly responsible for the IR emission, is extremely red ($B - K = 5.2$). The LW3 flux shows a strong excess and indicates $SFR = 67 M_\odot yr^{-1}$. The source is also detected in the radio at 1.4, 2.5 and 4.9 GHz (Mann et al., 2002).

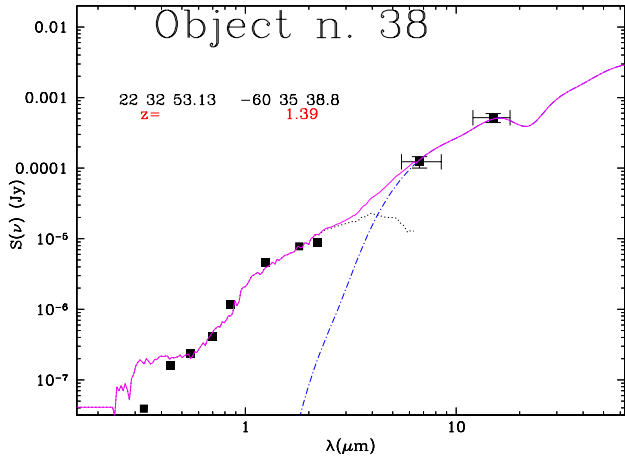


Fig. A.1. Spectral Energy Distribution of the object *s38*. The optical–NIR datapoints are fitted by normal spiral synthetic spectrum obtained with GRASIL (thin solid line, see sect.4.4), while the ISOCAM mid-IR data are fitted by a type–II AGN spectral template (dot–dashed line). The latter assumes obscuration by an edge–on torus whose ratio between inner and outer radii is 300, and with an optical depth at $0.3 \mu\text{m}$ of $\tau_\nu=30$ (see Franceschini et al. 2002).

S25, outside the WFPC-2 frame, is associated with a likely interacting pair of galaxies on the EIS images. We assumed the optical counterpart to correspond to the brighter galaxy. Both optical counterparts have been observed in the high-res ISAAC mode by Rigopoulou et al. (2002), and were found to counter-rotate. H_α is resolved from [NII]. Optical and near-IR spectra consistently indicate a redshift of 0.58. Our photometrically-estimated baryonic mass is $\sim 10^{11}M_\odot$, to be compared with the total dynamical mass of $4 \cdot 10^{11}M_\odot$.

S27 was observed by Rigopoulou et al. (2000) and here with FORS2. H_α and H_β detections indicate $z = 0.58$. Rigopoulou et al. (2002) report results of high resolution ISAAC spectroscopy, providing a huge dynamical mass of $10^{12}M_\odot$. The optical SED is well fit by the M51 template, and yields to a mass of $4.5 \cdot 10^{11}M_\odot$. The WFPC-2 images show a prominent bulge and well evident regions of star-formation along the spiral arms. The moderately high LW3 flux suggests, however, that although this is one of the most massive spirals known with evidence of ongoing star-formation, overall it looks as a relatively quiescent galaxy (see Sect. 4.3).

S28 is a substantial, relatively blue, spiral at $z = 0.56$ (H_α from Rigopoulou et al., 2000), with a clearly defined and asymmetric spiral arm, possibly indicative of an interaction.

S38 has been observed by Rigopoulou et al. (2000), who detected the resolved H_α and [NII] lines. The line ratio is inverted ($[\text{NII}]\lambda 6583 > H_\alpha$), indicating a kind of type-II AGN activity. The object is detected at both $15 \mu\text{m}$ and in LW2 at $6.7 \mu\text{m}$: the comparatively large

value for the latter also clearly indicates an AGN contribution. If we assume the IR spectrum of a type-II quasar (Franceschini et al. 2002) fitting the LW3/LW2 ratio (see Fig. A.1), the 8 to $1000 \mu\text{m}$ luminosity becomes $L_{IR} = 2.72 \cdot 10^{45} \text{erg s}^{-1}$. The very red optical source shows an almost point-like core with a very faint diffuse extension (Fig. A.2). The moderate broadness of the H_α and the red optical colors suggest a type-II AGN nature.

S39 at $z=1.27$ is the most luminous ULIRG ($L_{IR} = 4.4 \cdot 10^{12}L_\odot$) among the sources in our sample. It is a radio source detected at 1.4 GHz. The WFPC-2 morphology becomes more and more point-like at increasing wavelengths, from U to K (Mann et al., 2002). The WFPC-2 image shows a spiral structure with a bright nuclear extended emission, a kind of compact bulge. Rigopoulou et al. (2000) detect H_α at $z = 1.27$, with marginal evidence for broadening ($1200 \pm 450 \text{ Km/s}$). The LW3 flux, assumed it is due to a starburst (but an AGN contribution is also possible, see Sect. 4.1), leads to a very high value of $SFR \simeq 750 M_\odot \text{ yr}^{-1}$.

S40 is a strongly disturbed spiral showing three hot spots, likely starbursting regions, in the HST image. H_α is detected in the ISAAC low-resolution spectrum at $z = 1.27$. The optical SED is very well fit by the M51 template, yielding a large baryonic mass of $\simeq 2.2 \cdot 10^{11}M_\odot$. The LW3 flux shows a very large excess, indicative of an actively starforming galaxy with $SFR \simeq 265 M_\odot \text{ yr}^{-1}$.

S43 is outside the HST field. H_α is detected in the ISAAC 2000 run at $z = 0.95$ (the line was not detected by Rigopoulou et al. [2000] because of a poor estimate of the photometric redshift). The optical spectrum is well fit by M51, with a large mid-IR excess.

S53 is a beautiful double system with clear signs of interaction. Rigopoulou et al. (2000) published the near-IR spectrum of the brighter component. In the optical spectra we can deblend two components of H_β , at $\Delta\lambda \simeq 30 \text{ \AA}$ with EMMI and $\Delta\lambda \simeq 25 \text{ \AA}$ with FORS2. These values yield to a difference in radial velocity between the two galaxies of about 500 km/s. The brighter galaxy shows a well-defined circum-nuclear ring caused by a previous high-velocity encounter with the smaller galaxy. This latter shows in turn a faint off-center spot on top of a low-surface brightness emission. The redshift measured by Rigopoulou et al. (2000) and confirmed here is $z = 0.58$. The optical SED is rather blue, not well matched by the M51 template (the mass estimate is based on a fit with refined spectrophotometric model).

S55 is identified with another double interacting optical source, including a large spiral and a seemingly spheroid. H_α has been detected by Rigopoulou et al. (2000) in ISAAC low-res and medium-res at $z = 0.76$, and H_β with FORS2 observations. The optical-UV SED is reasonably well reproduced by M51. The high resolution spectrum reveals an “S”-shaped H_α emission, and allows a dynamical mass estimate consistent with our photometric estimate (see Table 6).

S60 is the IR counterpart of a high-redshift spiral galaxy with a possibly interacting counterpart showing

some evidence of interaction (a tail). It has been observed by Rigopoulou et al. (2000) who detected H_α at $z = 1.23$. The overall spectrum is fairly well fit by the M51 template, with only a moderate enhancement of the LW3 flux. The galaxy then appears to be moderately active in forming stars. However, its photometrically-determined mass appears to be enormous ($\sim 5 \cdot 10^{11} M_\odot$), and similar as such to the other system of source S27, apart from the much larger redshift. Its luminosity and $SFR \simeq 265 M_\odot yr^{-1}$ are in the ULIRG regime.

S62 was observed with ISAAC by Rigopoulou et al. (2000), who detected H_α at $z = 0.73$. The source appears moderately blue in the optical and quite active in the mid-IR.

S72 was observed during the ISAAC 2001 run with H_α detected at redshift $z = 0.55$. The galaxy is an edge-on spiral in an apparently rather crowded field, but not much spatial detail is available in the WFPC-2 image. The optical SED is quite red, possibly due to inclination. The overall SED is very well fitted by the M82 template.

S73 is a very large nearby spiral galaxy with satellites. The H_α line emission is detected in the FORS2 spectrum at $z = 0.17$. The SED has been fitted by us with the GRASIL library, the mid-IR spectrum showing excess activity compared with an inactive spiral. The WFPC-2 image shows a spiral with very well developed arms and a bar. Radio emission at 1.4 and 2.5 GHz is reported by Mann et al. (2002).

S79 H_α line emission at $z = 0.74$ was detected in this source during the ISAAC 2000 run. The optical SED matches that of M51, but shows a large excess above it in the mid-IR.

S82 consists of two rather symmetric optical sources, one of which almost point-like and the other slightly more extended, but with no much evidence of disk-like or otherwise diffuse emission. Observed with ISAAC in 2000, its spectrum yields H_α at $z = 0.69$. The optical SED is peculiar, with a sharp change in slope in the I band. The small LW3/LW2 ratio may indicate the presence of an AGN in one or the other of the optical counterparts.

This figure "2915f1.jpg" is available in "jpg" format from:

<http://arxiv.org/ps/astro-ph/0303223v1>

This figure "fran2915_pag26.jpg" is available in "jpg" format from:

<http://arxiv.org/ps/astro-ph/0303223v1>

This figure "fran2915_pag27.jpg" is available in "jpg" format from:

<http://arxiv.org/ps/astro-ph/0303223v1>

This figure "fran2915_pag28.jpg" is available in "jpg" format from:

<http://arxiv.org/ps/astro-ph/0303223v1>

This figure "fran2915_pag29.jpg" is available in "jpg" format from:

<http://arxiv.org/ps/astro-ph/0303223v1>